Investigation of Using Diffuse Gamma Simulations for the Generation of 3D Background Models

Master's Thesis in Physics

Presented by

Marco Egelkraut

July 12, 2021

Erlangen Centre for Astroparticle Physics
Friedrich-Alexander-Universität Erlangen-Nürnberg

Supervisor: Prof. Dr. Christopher van Eldik

Abstract

In the recent years, the three-dimensional (3D) likelihood analysis of data from Imaging Atmospheric Cherenkov Technique (IACT) γ telescopes experiences a growing reception, connected to the growing popularity of Gammapy. This describes the usage of spectral and spatial source models in combination with a 3D background model which is fitted to the observed data. These models are then able to describe the spatial and energy distribution of the observed events over the whole Field of View (FoV). In contrast, most of the background estimation techniques used by classical analyses derive the background from source-free regions in the FoV. In regions which are contaminated by diffuse gamma emission or many gamma sources, this is not always possible. As of now, 3D background models are constructed using real observations, ideally pointing towards regions with few gamma sources. However, such sky regions are typically providing hardly new insights, reducing the available observation time for the actual regions of interest. This could be avoided by constructing these background models using simulated data. The goal of this thesis is to generate a background model by using diffuse γ simulations and assess its quality. In the course of this work, the simulated background model is compared to a standard one, generated by L. Mohrmann et al. [1]. Furthermore, the performance of the generated background model in Gammapy analyses of two point-sources is evaluated. Overall, it was found that the simulated background has some weak points, but the resulting analysis results of the two point-sources are very similar.

Zusammenfassung

Die dreidimensionale (3D) likelihood Analyse von IACT γ Teleskopen gewinnt in den letzten Jahren immer weiter an Bedeutung, dies zeigt sich auch in der steigenden Verbreitung von Gammapy. Bei dieser Analysetechnik modelliert man die beobachteten Ereignisse durch die Nutzung von räumlichen und spektralen Quellmodellen sowie einem 3D Hintergrundmodell. Zusammen beschreiben diese Modelle die räumliche Verteilung und das Spektrum der beobachteten Ereignisse über das gesamte Teleskopsichtfeld. Im Gegensatz dazu nutzen die Hintergrundabschätzungen von klassischen Analysetechniken quellfreie Teile des Sichtfelds zur Bestimmung des Hintergrunds. Dies ist aber nur möglich, wenn das Sichtfeld weder diffuse γ Emission, noch zu viele Quellen enthält. Diese Voraussetzungen sind gerade für das galaktische Zentrum oft nicht erfüllt. Solche quellfreien Observationen werden zurzeit auch benötigt, um 3D Hintergrundmodelle zu erstellen. Da die Beobachtung dieser quellfreien Regionen aber oft kaum neue Erkenntnisse liefert, beschränkt dies die für die eigentlichen Zielregionen verfügbare Zeit deutlich. Das könnte verhindert werden, indem man die Hintergrundmodelle mittels simulierter Daten erstellt. Das Ziel dieser Masterarbeit ist es, ein Hintergrundmodell mittels simulierten diffusen Gammastrahlen zu erstellen und die Qualität von diesem zu beurteilen. Dazu wird das erstellte simulierte Hintergrundmodell mit dem Standardmodell von L. Mohrmann et al. [1] verglichen und das Verhalten der Hintergrundmodelle in Gammapy Analysen von zwei Punktquellen evaluiert. Bei der Vorhersage des γ Hintergrunds wurden für das simulierte Modell einige Schwachpunkte gefunden, die Ergebnisse der Punktquellenanalysen sind aber sehr ähnlich.

Contents

1 Introduction

Even before centuries, mankind was fascinated by the stars and the night sky in general. This fascination led to the development of more and more advanced observation techniques, like telescopes in the 17th century. All these techniques suffer one common limitation: They cannot influence the measured objects. For this reason, astronomers from all around the world are trying to use all available information to describe the universe correctly. One example of this effort is the Laser Interferometer Gravitational-Wave Observatory (LIGO), which was the first experiment to succeed in detecting gravitational waves.

Another interesting approach to gather information is gamma astronomy. Where the normal telescopes use light in the visible spectrum, gamma astronomy focuses on gamma photons with energies of several MeV and above. This thesis focuses on Very High Energy (VHE) photons with an even higher energy range of 100 GeV and beyond.

1.1 Direct Approach and the Imaging Atmospheric Cherenkov Technique

To conduct gamma astronomy, one must detect the energy and the direction of incoming gamma photons. One obvious approach is to do this directly, for example by using scintillation detectors. As the atmosphere is not transparent for gamma photons, these measurements must be conducted in space. Currently, this is done by Fermi Gamma-ray Space Telescope (Fermi), covering photon energies between 20 MeV to 300 GeV.

As the incoming flux of photons located in the VHE domain decreases strongly, a reasonable number of detected events can only be reached by increasing the detection area. This is problematic for the space bound approach, as this would be very expensive, or at some point even impossible.

One possible solution for this problem is to use an indirect approach, in this case the IACT. This technique is based on the following decay chain:

1. When a VHE photon enters the atmosphere, it can convert into an electron and a positron. This process is called pair production. However, this process can, because of the conservation of momentum, only happen in the vicinity of another reaction partner, typically a nucleus. That prevents the pair production to occur in space, enabling the gamma photon to reach the solar system unchanged.
2. The resulting electron and positron are then travelling further towards the earth's surface. Generally, during their movement, they interact with the surrounding matter. For high energies, the typical process is the generation of Bremsstrahlung. High energetic electrons and positrons emit Bremsstrahlung when they are accelerated. This happens in Coulomb fields of nearby particles.
3. The emitted Bremsstrahlung photons can then again lead to electron-positron pair

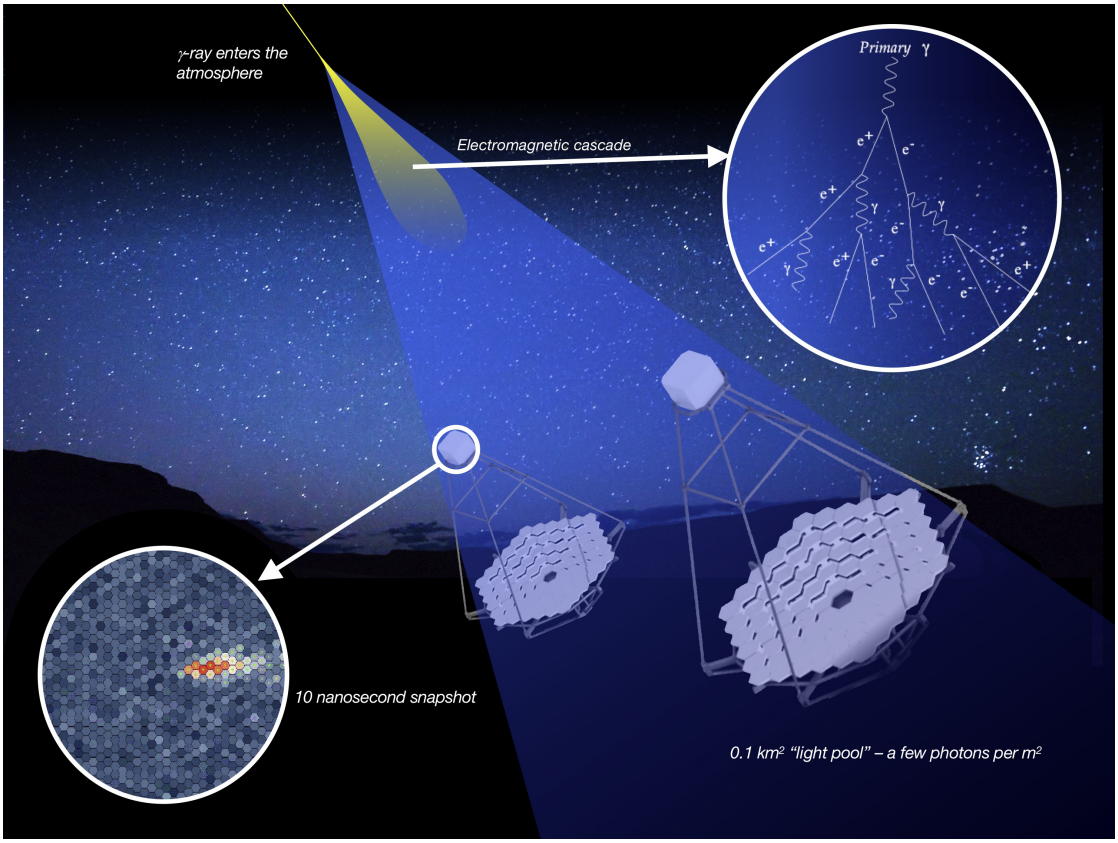

Figure 1: Artistic depiction of a Cherenkov light cone, detected by two IACT telescopes. A typical telescope image is shown in the bottom left corner. In the top left corner, one can see an illustration of the particle cascade.
Credit: R. White (MPIK) / K. Bernlohr (MPIK) / DESY

production, providing that their energy is sufficient (at least 1022 MeV). That constitutes a cyclic process, doubling the number of particles with each iteration.

This decay is a simplified model of the interaction of VHE photons with matter [2, pp. 386 sqq.]. In the atmosphere, this process generates a so-called cascade or air shower.

To detect this shower, one uses the emitted Cherenkov light. Cherenkov light is emitted, when particles are traversing a medium with a velocity larger than the local speed of light. The energy threshold for this can be calculated by using the Lorentz factor γ and the local refractive index $n(h)$ [3, pp. 330 sqq.]:

$$\gamma \geq \frac{n(h)}{\sqrt{n(h)^2 - 1}} \tag{1}$$

The refractive index in dependency of the height h can be approximated by the following

function:

$$n(h) = 1 + 0.000283 \frac{\rho_{\text{air}}(h)}{\rho_0(h)} \tag{2}$$

Using the refractive index $n(h)$, one can calculate the angle between the emitted Cherenkov light and the direction of the corresponding particle:

$$\cos(\theta_{\text{Ch}}) = \frac{1}{\beta \cdot n(h)} \quad \text{with} \quad \beta = \frac{v}{c_{\text{vac}}} \tag{3}$$

"Typical values at $h = 10\,\text{km}$ are $\theta_{\text{Ch}} = 0.8°$ and a threshold of $\gamma = 72$, corresponding to $E = 37\,\text{MeV}$ for electrons [and positrons] and $E = 7.6\,\text{GeV}$ for muons. The Cherenkov light cone of a particle at 10 km height has a radius of about 120 m at ground." [3, p. 331]

This generated light cone can then be detected on earth. A typical telescope's image of an air shower can be seen in Figure 1. The energy of the initial particle can be estimated by measuring the number of photons associated to the particle shower. This number is proportional to the number of particles in the air shower, which is proportional to the energy. As a rule of thumb, one can assume that $100\,\text{Photons/m}^2\text{TeV}$ reach the earth at a sea level of 2 km [4, p. 15]. Using this indirect approach, a modern telescope can cover an effective detector area of approximately $10^5\,\text{m}^2$ [5, p. 1].

Figure 2: Picture of the High Energy Stereoscopic System (H.E.S.S) site, containing its five telescopes. Image credit: [6].

1.2 The High Energy Stereoscopic System

In this thesis, data from the High Energy Stereoscopic System (H.E.S.S) is used. H.E.S.S is a IACT gamma observatory built in 2002/2003. It is composed of four telescopes with a flat-to-flat mirror diameter of 13 m (CT1 to CT4) and an effective mirror area of 107 m^2, providing a FoV of 5°. These telescopes are arranged in a square with a distance of 120 m to each other. These telescopes provide a roughly uniform response function for the innermost 2° of their FoV. In 2012, H.E.S.S was extended by a larger fifth telescope, it has an effective mirror area of 614 m^2. The setup before this extension is called Phase 1, the subsequent one Phase 2. This thesis uses Phase 1 data. [7]

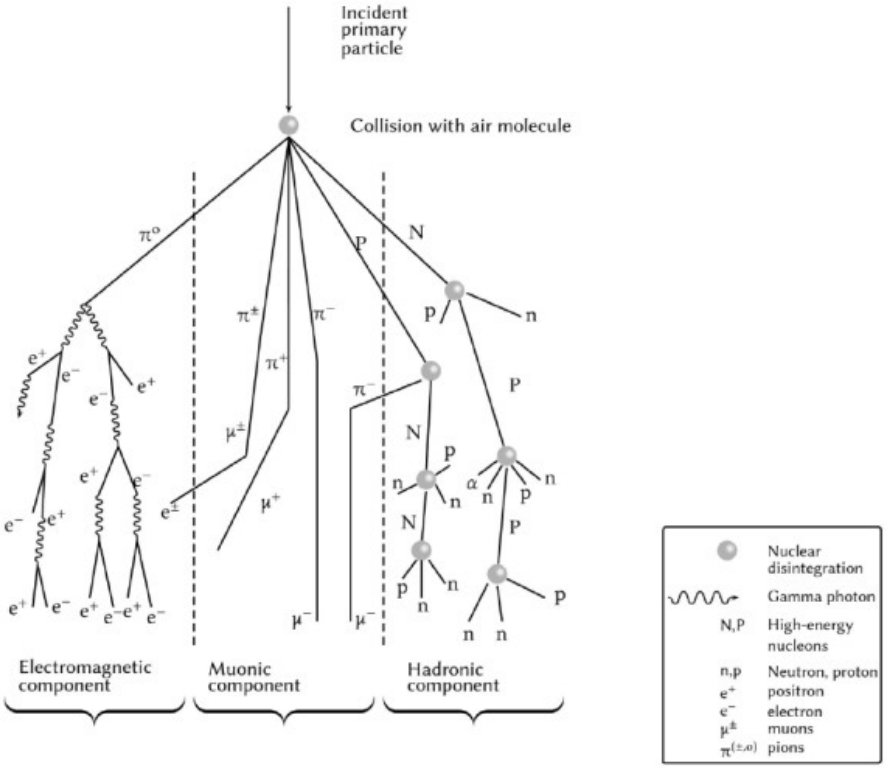

Figure 3: Air shower generated by a hadronic particle. Air showers of this type can be observed by IACTs and must be discriminated against showers from photons. Image from [8].

1.3 Air Showers Generated by Hadrons

One problem of the IACT is, that incoming hadronic particles can generate similar particle cascades. This is shown in Figure 3. When an incoming particle interacts with the atmosphere, it can decay mainly into pions, kaons, nuclear fragments and neutrinos [9, pp. 33 sqq.]. One possible decay product is the neutral pion π^0, which, in most cases, decays after a short mean life time of $(8.52 \pm 0.18) \times 10^{-17}\,\mathrm{s}$ into two photons [10, p. 38]. These two photons can than start gamma air showers.

The charged pions $\pi^{\pm}$ decade into muons $\mu^{\pm}$ and neutrinos. As of their larger lifetime of $2.6 \times 10^{-8}\,\mathrm{s}$, there is the possibility that they interact with other atmospheric particles before they can decay. This can start new hadronic subshowers.

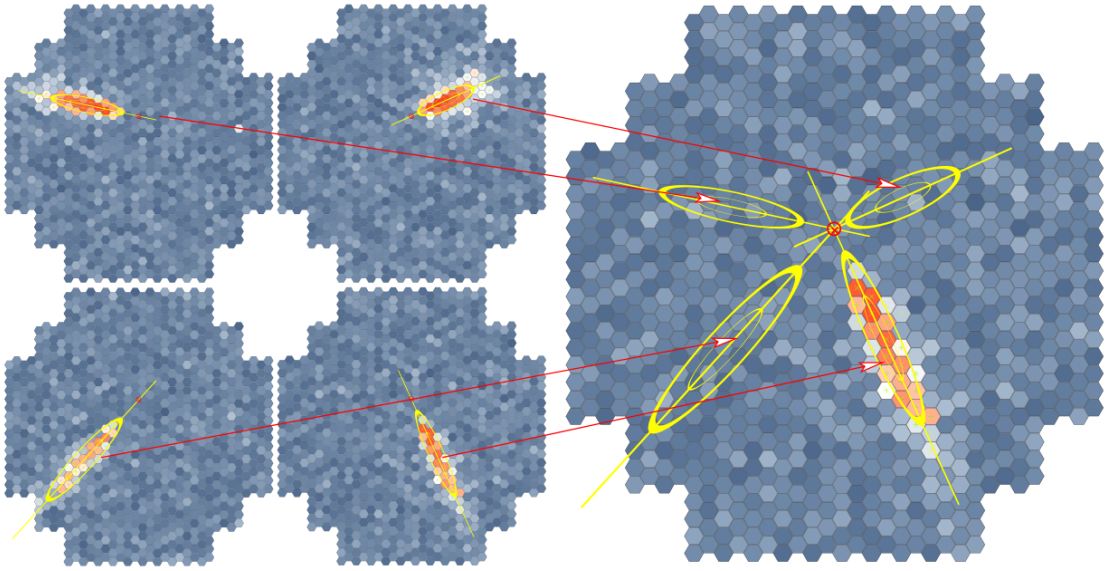

Figure 4: On the left side, one can see the images from four telescopes of one common air shower. The respective air showers are modelled by an ellipse. When these ellipses are drawn into one camera plane (right side), the origin of the primary particle can be estimated by the intersection point of the four major axes of the ellipses. Image from K. Bernlöhr [11].

1.4 Reconstruction of Air Showers and γ/Hadron Separation

After the detection of an air shower's Cherenkov light by IACT telescopes, the gathered information must be processed, so that the origin, the type and the energy of the primary particle can be estimated. Typical images of a γ air shower can be seen Figure 4. As shown in the image, typical air showers can be modelled by ellipses. As the air showers follow approximately the path of the primary particle, the origin of the primary particle must lie on the ellipse's major axis. By combining an event's images from multiple telescopes into one common camera plane, the direction of the primary particle can be estimated by the intersection point of the major axes.

Another important point is to determine the type of the primary particle. This step is also called *gamma*/hadron separation. For this step, one can use the Hillas parameters of an air shower image, as proposed by A.M. Hillas in 1985 [12]. For γ/hadron separation, one usually uses the following:

- The *width* and *length*. These parameters describe the variance of the photon distribution perpendicular and parallel to the major axis.
- The *image amplitude*. This is the sum over all pixel counts in the cleaned image.
- The *nominal distance*. This is the angular distance between the centre of the air

shower's image and the camera's pointing position.

As introduced by Aharonian et al. [7], one can define two new conclusive parameters, the Mean Reduced Scaled Width (MRSW) and the Mean Reduces Scaled Length (MRSL). They are based on the Hillas parameters: [13, pp. 42 sq.]

$$\mathrm{MRSW} = \frac{1}{N_{\mathrm{tel}}} \sum_{\mathrm{tel}} \frac{w - \langle w \rangle}{\sigma_w} \tag{4}$$

$$\mathrm{MRSL} = \frac{1}{N_{\mathrm{tel}}} \sum_{\mathrm{tel}} \frac{l - \langle l \rangle}{\sigma_l} \tag{5}$$

Here, w and l are the Hillas parameter *width* and *length*, whereas $\langle w \rangle$ and $\langle l \rangle$ denote the expected value for γ showers with the same *image amplitude*, zenith angle and impact distance. Those expectation values are gathered from Monte Carlo simulations. The impact distance describes the distance between the position of the telescope and the imaginary intersection of the primary particle's path and the ground.

This impact distance, combined with the *image amplitude*, the zenith angle, the optical efficiency and the *nominal distance*, can also be used to reconstruct the energy of the primary particle. This is done by searching for simulated air shower images with similar property values. This can be simplified by using the simulations to generate a look-up table for the above mentioned parameters [13, p. 40].

One simple possibility to separate γ from hadron air showers is to use cuts on the mentioned parameters. However, in this thesis, a more sophisticated approach is used. The applied method is based on Boosted Decision Trees (BDT), as described by S. Ohm, C. van Eldik and K. Egberts [5]. The training phase starts by generating one single decision tree. That is done by choosing subsequently this parameter, which separates the training data in the best way. This was done until the number of events in one node fell below $N/(10 \cdot N_{\mathrm{par}}^2)$. Here, N is the size of the training data set and N_{par} is the number of training parameters. Following training parameters were used [5]:

- MRSL and MRSW
- Mean Reduces Scaled Length Off (MRSLO) and Mean Reduced Scaled Width Off (MRSWO). These parameters are calculated the same way as above but use the expectation values of hadron air showers.
- The shower maximum X_{max}. This is the height of the position, where the number of the air shower's particles is maximal. X_{max} is the weighted mean of the telescope values.
- The average spread in energy reconstruction $\Delta E/E$ between the triggered telescopes. This is based on the irregularity of hadron air showers, possibly causing telescopes to reconstruct the shower energy differently.

The distribution of these parameters for γ and hadron air showers can be seen in Figure 5. However, one disadvantage of single decision trees is their instability against statistical

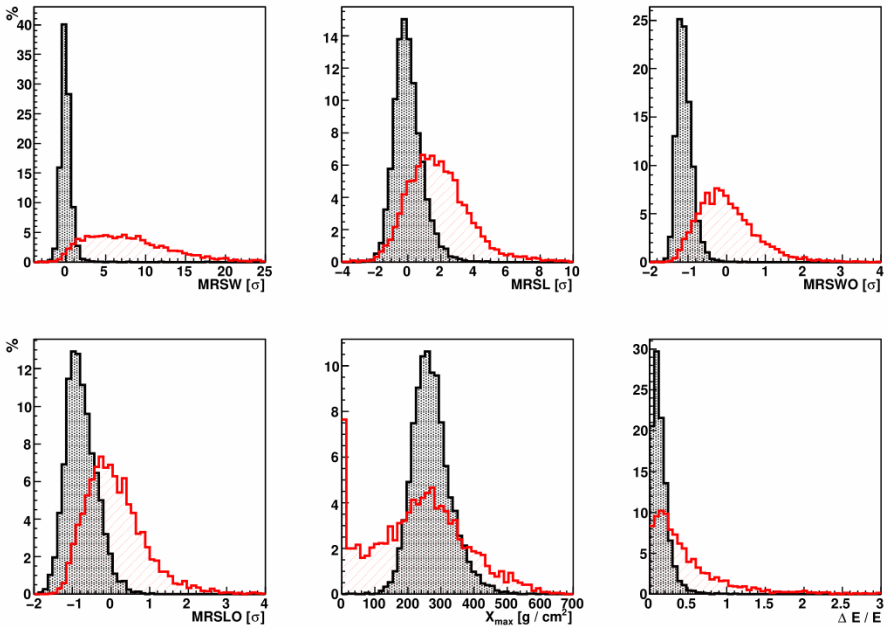

Figure 5: Distribution of the training parameters for γ-rays (black) and cosmic rays (red). For this figure, events with a reconstructed energy of 0.5 TeV to 1 TeV and zenith angles in the range of 15° to 25° were used. Reprinted from [14]

fluctuations in the training data set. This effect can be reduced by "boosting" the decision tree. That means, that a new decision tree is generated using a reweighted training data set: The weights of previously misclassified events are increased by multiplication of a factor α, leading to a slightly changed decision tree. That procedure is repeated multiple times, always based on the last generated decision tree. This boosting routine is called *AdaBoost*, it uses a factor of $\alpha = (1 - \text{err})/\text{err}$. Here, err is the probability of an event being misclassified by the previous decision tree.

The boosting procedure generates a "forest" of decision trees. It is evaluated by calculating a weighted mean of the single trees' results. The mean is than called ζ. One remaining problem of this approach is, that some training parameters (the shower maximum $X_{\max}$ and the average spread in energy reconstruction $\Delta E/E$) are energy and zenith angle dependent. This impairs the quality of the BDT γ/hadron separation. That can be counteracted by dividing the events into zenith angle and energy bins. Then, a BDT is generated for each bin. However, this can lead to a discontinuous behaviour at the bin boundaries.

In this thesis, data with the configuration "std_zeta_fullEnclosure" is used. It classifies an event's primary particle as γ photon, if ζ is in the range of 0.00 to 0.84. Additionally, it uses some preselection cuts, preventing poorly reconstructed events from being evaluated by the BDT. A typical ζ distribution for one specific bin ($E_{\text{rec}} \in [0.5, 1.0]$ TeV; zenith angle $\in [15, 25]°$) can be seen in Figure 6. One can see that this γ/hadron separation cannot

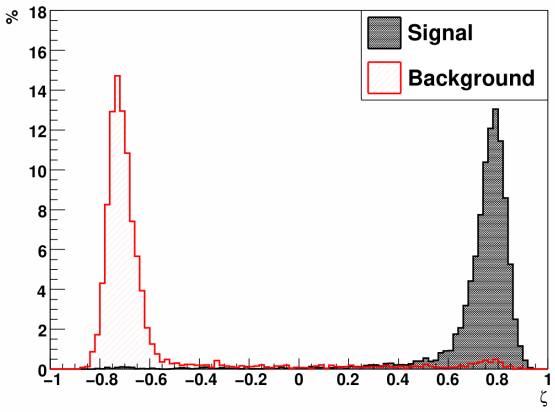

Figure 6: Typical distribution of the ζ parameter in an independent validation dataset for one specific energy/zenith angle bin (as specified in Figure 5). Reprinted from [14]

filter out hadron events completely, especially as they are typically more frequent than γ events. The small right peak indicates that there is a type of hadron air showers which are very similar to γ showers. Consequently, this type is frequently misclassified.

1.5 Background Estimation

As described before, the γ/hadron separation alone is not able to filter out hadron events completely. This makes it necessary to use additional methods to estimate the remaining background. In the following, some typical methods are described.

1.5.1 Simple On/Off Techniques

One simple approach to estimate the background of an image is to use simple On/Off techniques. This refers to whether an observation contains a γ-ray source (On/Off source observation). The background of two observations from the same telescope can be approximated to be identical, if they have comparable Altitude/Azimuth pointing positions, optical efficiencies, and atmospheric conditions. For the latter one, the respective on/off runs are typically conducted immediately consecutive. [15]

However, this has the disadvantage, that only half of the available measurement time can be used to observe the actual planned sky regions. Another problem is to find suitable off-source sky regions. Especially in the galactic plane this is sometimes not possible.

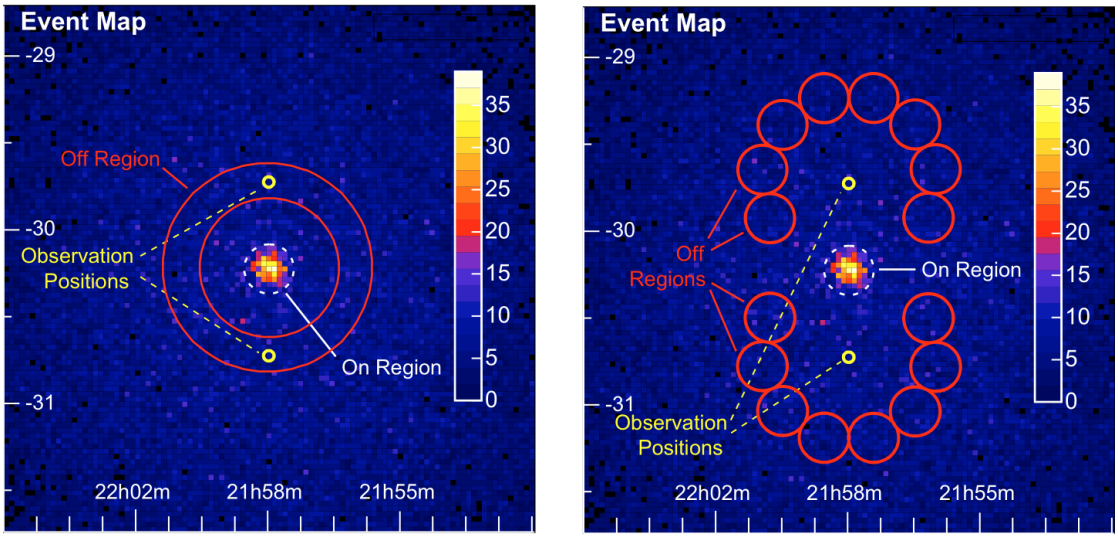

Figure 7: Illustration of the ring background and reflected background method. In the ring background method (left), the off region is chosen to be a ring around the on region. For the reflected background method (right), off regions with a similar shape and distance to the centre of the image are chosen. Image from [15].

1.5.2 Ring Background and Reflected Background

Simple On/Off techniques, as described above, are based on the requirement, that the On and Off region have the same detector acceptance. The main disadvantage of this is, that this requirement is only fulfilled for very specifically chosen Off regions. This can be avoided by introducing a normalisation factor α, compensating different detector acceptances:

$$N_{\text{source}} = N_{\text{on}} - \alpha N_{\text{off}} \tag{6}$$

In general, α can be calculated as following:

$$\alpha = \frac{\int_{\text{on}} A^{\gamma}_{\text{on}}(\psi_x, \psi_y, \Theta_z, E, t)\mathrm{d}\psi_x \mathrm{d}\psi_y \mathrm{d}\Theta_z \mathrm{d}E\mathrm{d}t}{\int_{\text{off}} A^{\gamma}_{\text{off}}(\psi_x, \psi_y, \Theta_z, E, t)\mathrm{d}\psi_x \mathrm{d}\psi_y \mathrm{d}\Theta_z \mathrm{d}E\mathrm{d}t} \tag{7}$$

In this equation, α is calculated by dividing the integrated acceptance of the on region over this of the off region. This integration is done over the FoV coordinates (ψ_x, ψ_y), the zenith angle Θ_z, the energy E and the time t. [15]

One method using this normalisation factor α is the ring background: Here, the off region is chosen to form a ring around the on region. An illustration of the ring background can be seen in Figure 7 (left). One advantage of this method is the correct handling of linear gradients in the FoV. However, the derivation of the normalisation factor α can introduce additional systematic errors.

One possibility to reduce these systematic errors is to simplify the calculation of α, as it is done in the reflected background method. For this method, the telescopes must not point directly towards the trial source position, rather a specific pointing offset must be used. For H.E.S.S, this value is typically 0.5°. As a consequence, it is possible to choose off-regions with similar shape and FoV distance from the centre of the image, as shown in Figure 7 (right). This enables it to approximate α to $1/n_{\text{off}}$, depending only on the number of off regions n_{off}. In general, the uncertainty of this method is decreasing if the number of off regions n_{off} is decreased. A disadvantage of both methods is, that additional sources in the FoV can make it difficult to find suitable off-regions. [15]

1.5.3 Background Model Templates

All previously mentioned background estimation models have in common, that they require suitable off regions which do not contain any sources. However, this is not always possible. One method which is not dependent on the number of sources in the FoV is the usage of background model templates, as described in [1]. These background model templates are 3D-background models, giving the expected background rate as a function of the two FoV coordinates and the reconstructed energy of the primary particle. As the background rate also depends on the altitude and azimuth angle of the observation, it is necessary to divide the possible pointing directions into bins. Then, for each bin, a specific background model template is used. In [1], two azimuth bins and eight zenith angle bins were used.

As the optical efficiency of telescopes degrades over time, a specific background model template can only be used for a limited period. To describe this degeneration of the optical efficiency, H.E.S.S uses different optical phases. The optical efficiency of observations in one phase can then be approximated to have one common value. In this thesis, all mentioned observations were taken in the optical phase 1b, they were taken in the years 2004 to 2007.

In principle, background model templates can be generated by adding up all measured events from observations located in one common altitude and azimuth bin. In this data, all sources must be masked. This masking can be compensated by also adding up the masked exposure time for each spatial pixel. Using this exposure time array, the background rate can then be calculated. The exact procedure is more extensive and is described in detail in [1].

The idea of this thesis is to generate such background model templates using simulated data. This would make the background estimation more independent from previous observations. Also, no observation time must be spent to gather information for the background model, which is an advantage if extended gamma sources are observed.

2 Monte Carlo Simulation of Diffuse γ Rays

The goal of this thesis is to validate the usage of Monte Carlo simulations of diffuse γ rays for the generation of background model templates. This background model should describe remaining hadronic events which were miss-classified by the γ/hadron separation, possibly caused by a dominating electromagnetic component of the hadronic air shower (see subsection 1.3). Since these events were miss-classified as γ air shower, one can assume that these miss-classified showers are very similar to them. This similarity is the reason for attempting to model the remaining background by diffuse γ rays.

2.1 Description of the used Real and Simulated Observations

To test if this approach is indeed justified, it was decided to begin with a comparison of the basic properties of the real background and a simulated one. The simulation of diffuse γ air showers was done using `CORSIKA 7.41` with the `IACT/ATMO` package version 1.48 (2014-02-26) [16]. The reaction of the telescope array to these air showers is then simulated by `sim_telarray` (version: 2014-12-18) [17]. Incoming γ rays were simulated in the energy range from 160 GeV to 500 TeV with an energy index of -2.7. The telescopes were simulated to point towards south (azimuth = 180°), the zenith angle was set to be 20°. The diffuse γ rays were set to originate in a cone of 3° radius around the pointing position. The simulation was set to imitate the H.E.S.S telescopes in the optical phase 1b. The simulation used 250 CPUs with four cores each for 24 h. All events generated by one core are then interpreted as one simulated observation. This should lead to 1000 simulated observations. However, only 974 of them were terminated successfully. The remaining 26 runs terminated due to different errors. Hence, they were ignored.

In general, the simulated runs were processed by `HAP` (hap-18-pl05 (revision: 1.64)), using the configuration `std_zeta_fullEnclosure`. In detail, this consists of the following steps:

1. Transforming the files generated by `sim_telarray` (`".simhess"`) to root files. This is done by `montecarloreader`.
2. Transforming the root files into `dst` files. For this, the program `analyse` in the directory `hdanalysis` is used.
3. These `dst` files can then be processed by the program "hap" in the "hddst" directory. The program was set to use no background. This step includes the γ/hadron separation. By using the `FITS` setup parameters, one can export the resulting event lists into `FITS` files. These were then used in this thesis.

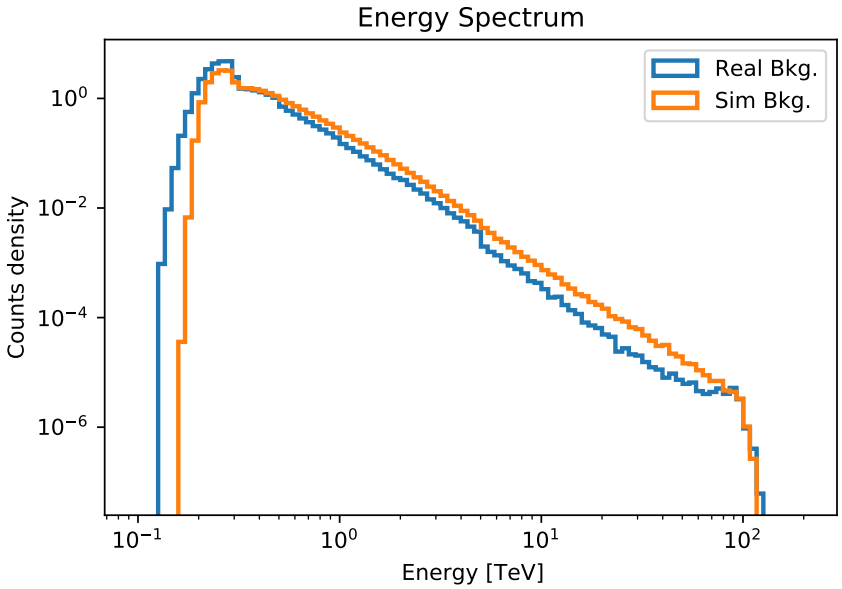

Figure 8: Comparison of the energy spectra of the real and simulated background. The sources in the real background were masked. The spectra are similar, but there are deviations: The simulated spectra starts at a higher energy. Also, at the BDT bin edge at 5 TeV the real spectrum is decreasing significantly, whereas the simulated one is hardly influenced.

2.2 Energy Spectrum of the Real and Simulated Background

At first, the energy spectrum of real and simulated background events is compared. This is done for the zenith angle bin of 15° to 25°, using simulations with a zenith angle of 20°. For this task, the simulated events are easily accessible. However, for the real observations, the mean background must be estimated at first. For this estimation, runs with a pointing towards the Galactic plane ($|l| < 60°$, $|b| < 5°$) have to be discarded, as they could contain diffuse γ emission. Additionally, discarded were runs with hardware failures, bad atmospheric conditions and with less than four operating telescopes. That procedure was previously described by L. Mohrmann et al. [1]. In combination with the desired altitude and azimuth bin ($15° \leq \text{alt} < 25°$ and $90° \leq \text{az} < 270°$) and optical phase (1b), the remaining number of observations is 504. This corresponds to a summed live time of 232.9 h. Then, the remaining sources were masked. To counteract the influence of the masking, the background rate was calculated using the summed exposure time for each spatial pixel. This process is also described in [1].

For the simulated background, no count rate can be calculated, as the time information is missing. Therefore, the counts density is compared. The resulting energy spectra can be seen in Figure 8. It was generated by summarising over all spatial bins. The energy spectrum of the simulated events starts at higher energies; thus, the remaining density curve is expected to be higher than the real background spectrum. Especially in the real energy spectrum, the discontinuities caused by the BDT training bins can be seen. This effect was described in subsection 1.4. It can be seen, that γ air showers are hardly affected compared to the hadron air showers. This leads to a decreased real energy spectrum above 5 TeV. Another difference is the behaviour around 0.4 TeV. Here, the simulated energy spectrum is decreasing slower than the real one. The last main difference is the behaviour at high energies, at 70 TeV and higher. In this region, the simulated spectrum is decreasing faster than the real counterpart.

Whereas the different impact of the BDT training bins can be explained by the different effect of the γ/hadron separation, the other differences have no obvious explanation.

2.3 Comparison of the Spatial FoV Distributions

Also important is the comparison of the spatial count distribution of the two backgrounds, it can be generated by summarising over the energy bins of the background. As a first step, the shape of the FoV distribution is shown in Figure 9. For this purpose, each colour plot displays the counts density in the respective FoV coordinate bin. Above and to the right of the colour plot, a projection of the count density onto the azimuth and altitude axis is shown. In order to avert disturbed contour lines caused by the coarse binning, the counts density was modelled by a Kernel Density Estimation (KDE) with a bandwidth of 0.18°. This model was then used to draw contour lines, improving the representation of the count distribution. The two contour lines of the same colour represent the same density value. Both plots use the same colour scale.

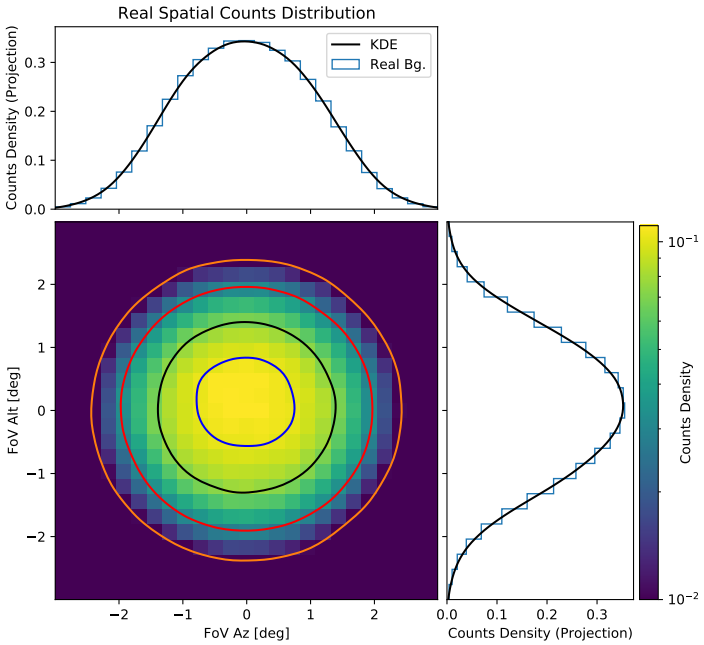

(a) Spatial counts distribution of background in real observations.

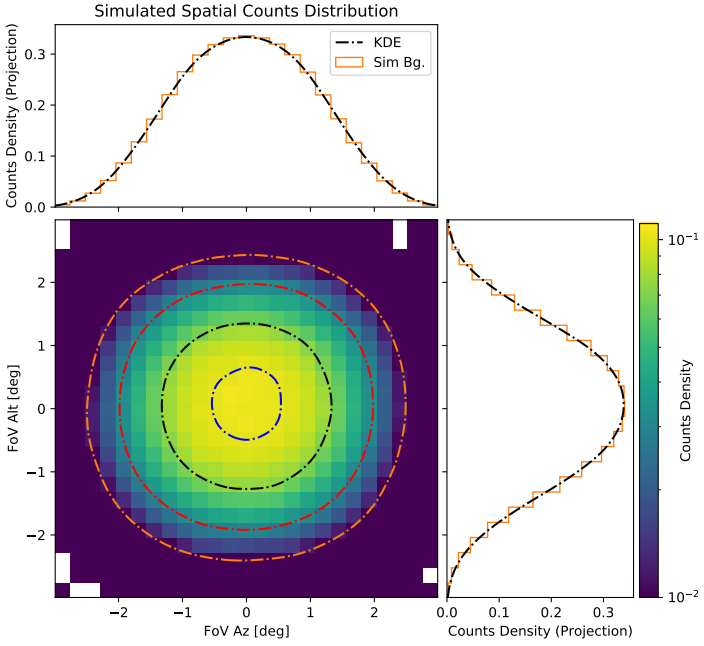

(b) Spatial counts distribution of the simulated background.

Figure 9: These two plots show the spatial counts density of the respective background. On the upper and right side of each colour plot, the counts density was projected onto the azimuth and altitude axis. The contours were generated by using a KDE. The respective projection of the KDE is also shown.

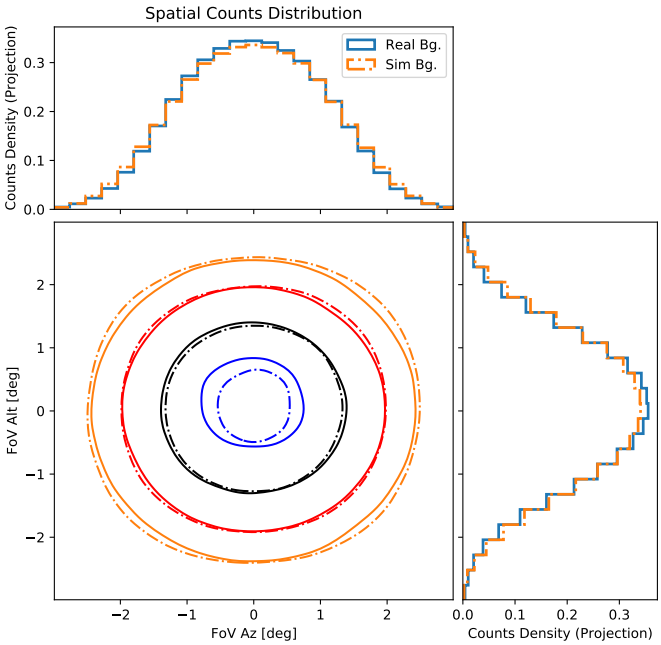

Figure 10: Here, the contour lines of the simulated and real background are plotted into a common coordinate system. Overall, they are in good agreement with one another. However, the simulated counts distribution is slightly broader than the real one.

As visible, the shapes of the count distributions are indeed comparable. For a more a precise statement, the two plots should now be combined into one representation. This can be achieved by using the contour levels. The result is shown in Figure 10. It can be observed that the simulated counts distribution is slightly broader than the real counterpart. However, the general shape of the count density is very similar. To describe the differences between the two backgrounds more accurately, a comparison function is introduced:

$$d = 2 \cdot \frac{r - s}{r + s} \tag{8}$$

It uses the real background density r and the simulated background density s. The result d of this function describes the difference between the two backgrounds over their mean value. In case of a perfect background model, this value should be equal to zero.

The resulting comparison function values d are shown in Figure 11. They support the hypothesis that the simulated counts distribution is broader than the real one. However, this trend is broken for the edge area of the FoV. Here, the real distribution is decreasing slower than the simulated one. One possible explanation for this effect is the configured origin region of the diffuse gamma rays in the simulation, a cone with a diameter of 3°. This value is a compromise between increasing the simulated area and limiting the required simulation time. Because of the reconstruction uncertainty, this limitation can

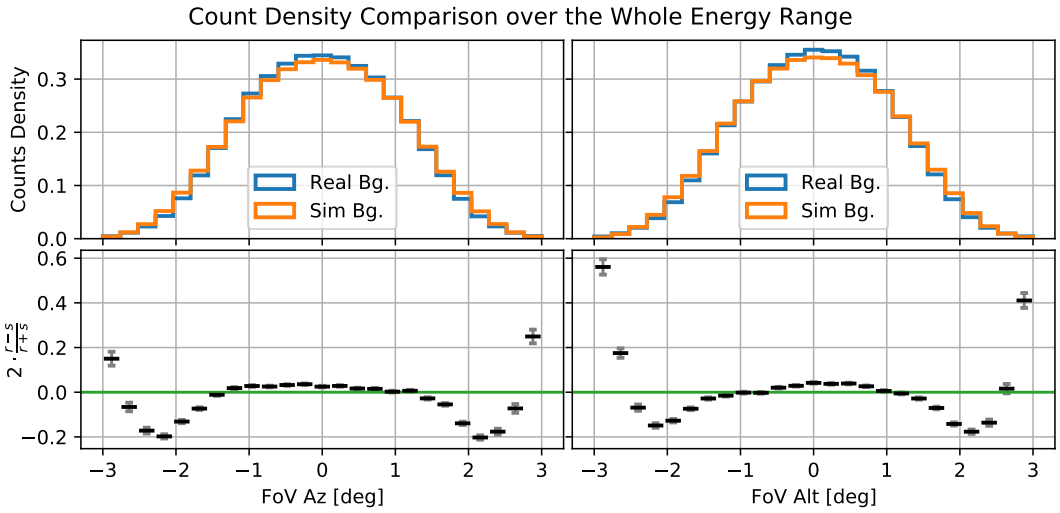

Figure 11: This figure shows the difference between the simulated and real background in a quantified way. The edge regions of the FoV exhibit larger deviations. In the centre region (up to a FoV radius of 2°), the simulated distribution is broader than the real one.

	$R = 1.0°$	$R = 1.5°$	$R = 2.0°$	$R = 3.0°$
FoV azimuth:	$(2.32 \pm 0.07)\,\%$	$(2.10 \pm 0.09)\,\%$	$(3.95 \pm 0.11)\,\%$	$(7.83 \pm 0.24)\,\%$
FoV altitude:	$(2.27 \pm 0.11)\,\%$	$(2.16 \pm 0.11)\,\%$	$(4.09 \pm 0.12)\,\%$	$(9.55 \pm 0.26)\,\%$

Table 1: Mean absolute deviations between simulated and real background in a given area around the centre of the FoV. If the radius of the compared area is increased beyond 1.5°, the resulting mean deviations are increasing.

also affect the bins with a radius smaller than 3°. As a later analysis would strongly depend on the centre of the FoV region, a good agreement between the simulated and real background is especially important there. The confinement of an analysis onto the centre region of the FoV is a common technique in gamma astronomy, as systematic effects at the edge of the FoV cannot be ruled out. One example for this is "The H.E.S.S Galactic plane survey" [18], there a FoV radius of $R = 2°$ is used. For different radii R, the mean of the absolute value of the deviation between the simulated and real background $\langle |d| \rangle$ can be seen in the Table 1. For each radius up to 2°, the mean deviation values $\langle |d| \rangle$ in azimuth and altitude direction are in good agreement with another. However, it can be observed that the deviations between the real and simulated background increase significantly beyond a FoV radius of 1.5°. For this reason, it seems appropriate to start later analyses with a limit on the FoV radius of $R = 1.5°$.

Another interesting point is to analyse the energy dependency of these deviations. For

this, the analysis energy ranged was divided into four bins. For each of these bins, the comparison function is plotted along the two spatial axes. This is shown in Figure 12. Except for the first energy bin from 0.10 TeV to 0.68 TeV, the simulated background is in the centre FoV region to high. For the edge regions of the FoV, the observed deviations show a different energy dependency: Here, the simulated background is always too low. If the deviations are compared to these of the plot of the whole energy range in Figure 11, it can be seen that the overall behaviour is dominated by the lowest energy bin.

These different energy dependencies are a reason to compare the resulting energy spectra of simulated and real background for different FoV regions. This is shown in Figure 13. It can be seen that a FoV radius smaller than 2° does not influence the respective energy spectrum. For a larger distance, the peak of each spectrum is decreased, whereas the probability of observing events with energies around 100 TeV is higher.

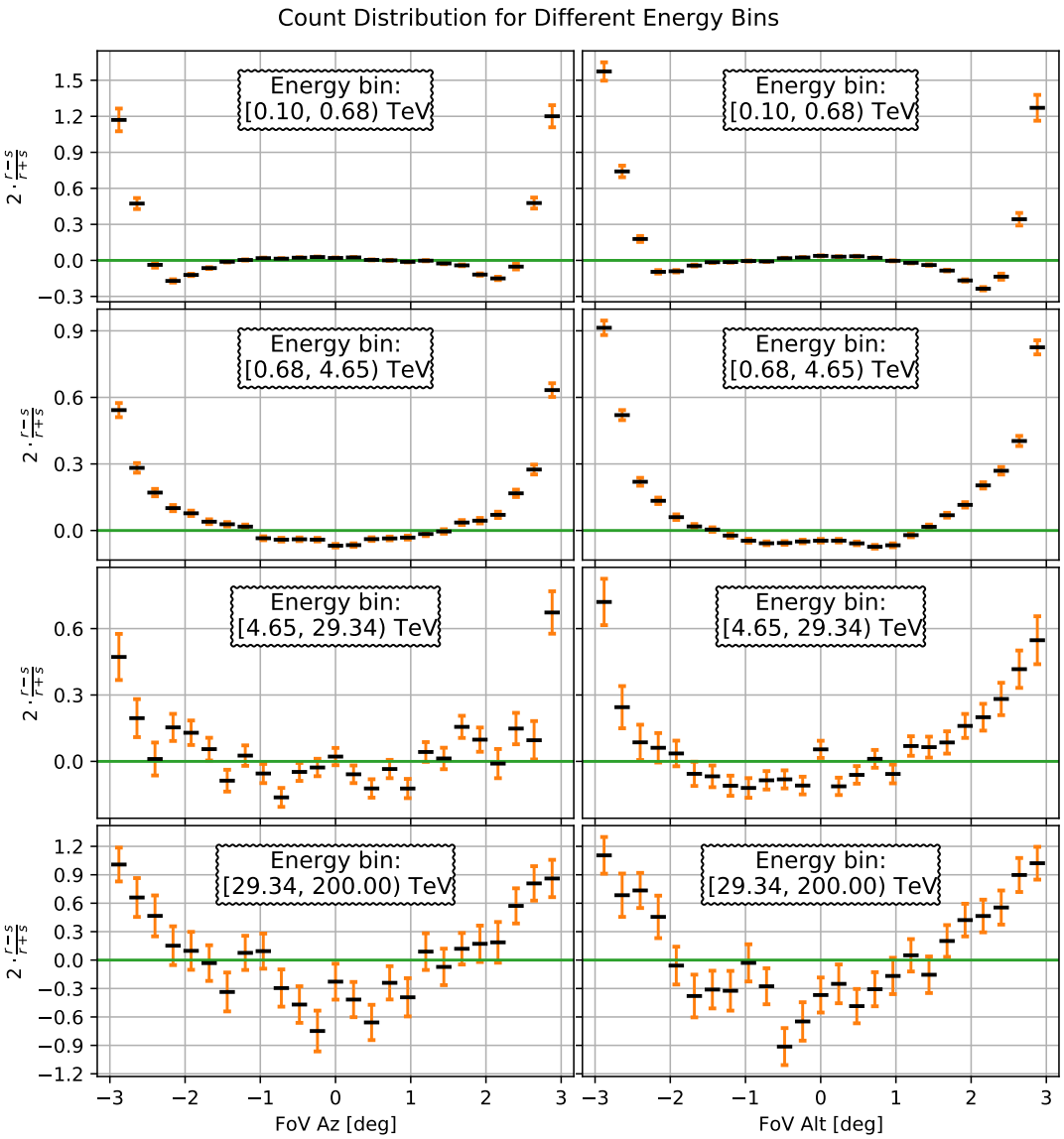

Figure 12: Comparison of the FoV distribution of events for different energy bins. Only for the lowest energies is the simulated background in the centre region too low, for all others it is too high.

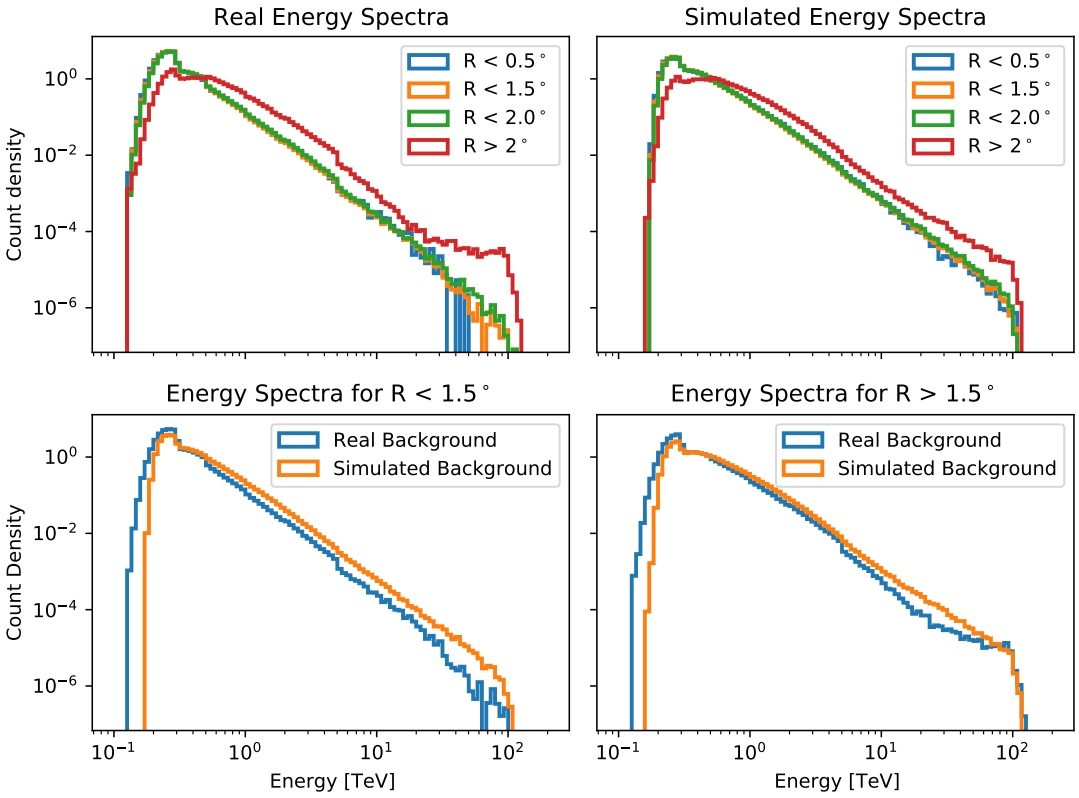

Figure 13: Energy Spectra for the simulated and real background for different FoV regions. It can be seen that the unexpected high spectrum for energies around 100 TeV is caused by the edge regions of the FoV. This effect is more distinct for the real energy spectrum. For radii smaller than 2°, the energy spectra of the two backgrounds are independent from the regarded FoV area. The lower two plots show a direct comparison between simulated and real background. As seen in Figure 8, the main difference between the real and simulated spectra, for the edge as well as the centre of the FoV region, is the dent above 5 TeV, caused by the different effect of the BDT training bin.

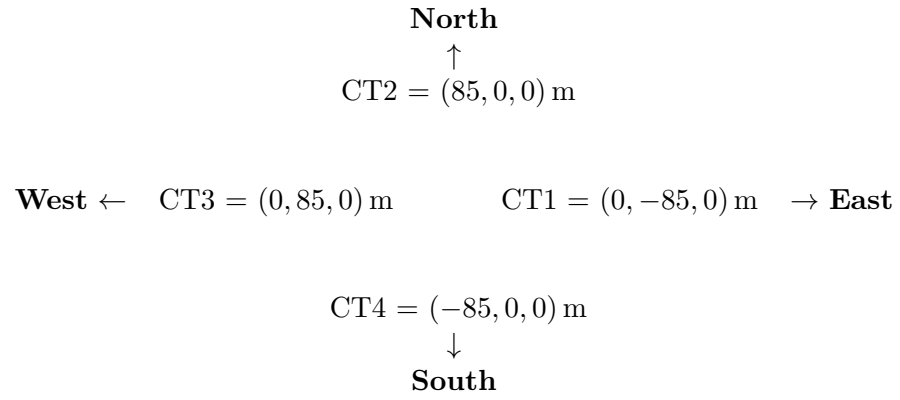

Figure 14: Arrangement of the four phase I H.E.S.S telescopes at the site in Namibia [19].

2.4 Comparison of the CORE Parameter

Closely linked to the spatial count distribution is the distribution of air showers' centre positions. Such a position corresponds to the imaginary point of impact of the primary particle. This parameter is important for reconstructing the shower energy, as it influences the measurement of an air shower's amount of emitted light. Compared to Monte Carlo simulations conducted by the H.E.S.S Collaboration, the RMS error of the impact position is smaller than 10 m, if the distance between the centre of the H.E.S.S array and the impact point is smaller than 200 m. [7]

The impact position can be stated by using the `"GroundSystem"`. The x-axis of this right-handed coordinate system points north, the y-axis east and the z-axis points upwards. As the impact points are per definition on the ground level, the z-coordinate is often omitted. The arrangement of CT1 to CT4 can be seen in Figure 14. Another important coordinate system for impact positions is the `"TiltedTelescopeSystem"`. Instead of the impact position itself, event tables do typically contain the projection of the impact position onto the xy-plane of the `"TiltedTelescopeSystem"`. This is then called CORE parameter. [19]

However, for the comparison of the CORE parameter, the procedure of masking the spatial position of gamma sources, as applied for the comparison of the spatial count distribution, is not applicable. The reason for this is, that the influence of masking of spatial regions on the CORE distribution cannot be compensated by adapting the region's exposure. Consequently, the selected run list had to be restricted, so that the remaining observations did not contain any known gamma sources in their FoV. From the previously used 504 observations, 138 are remaining. This number can be increased by also including phase 1d. It describes the H.E.S.S array after a recoating of all four mirrors, resulting in approximately the same optical efficiencies as phase 1b. After applying the

selection cuts described in subsection 2.1, phase 1d contains 84 observations, 44 of them do not contain any known gamma sources. The combined 182 observations cover a live time of 81.5 h.

The resulting spatial impact distributions are shown in Figure 15. Additionally, a direct comparison is shown in Figure 16 with the corresponding comparison values in Figure 17. The real CORE distribution is more blurred than the simulated one. In the latter, one can see the positions of the telescopes as peaks in the distribution. The other main difference is the general shape of the distribution: Whereas the real distribution resembles a circular shape, the simulated one is like a square. One possible explanation for these effects is, that the simulated multiplicity distribution is not correct. In this context, multiplicity describes the number of telescopes which one events has triggered. Independent from this, the real CORE distribution shows in its peak region a gradient towards the CORE x-axis. This could indicate that the optical efficiencies of the four telescopes are not, as modelled by phase 1b, equal.

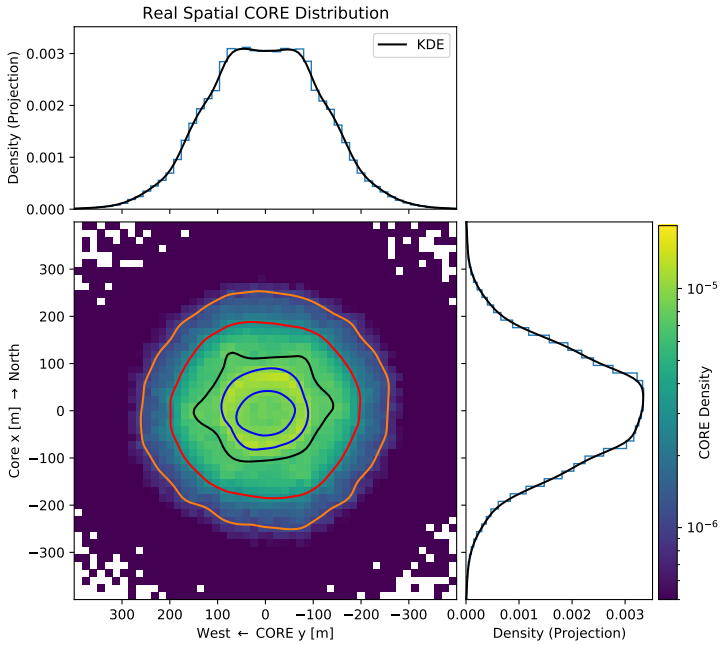

(a) CORE parameter distribution of real background events.

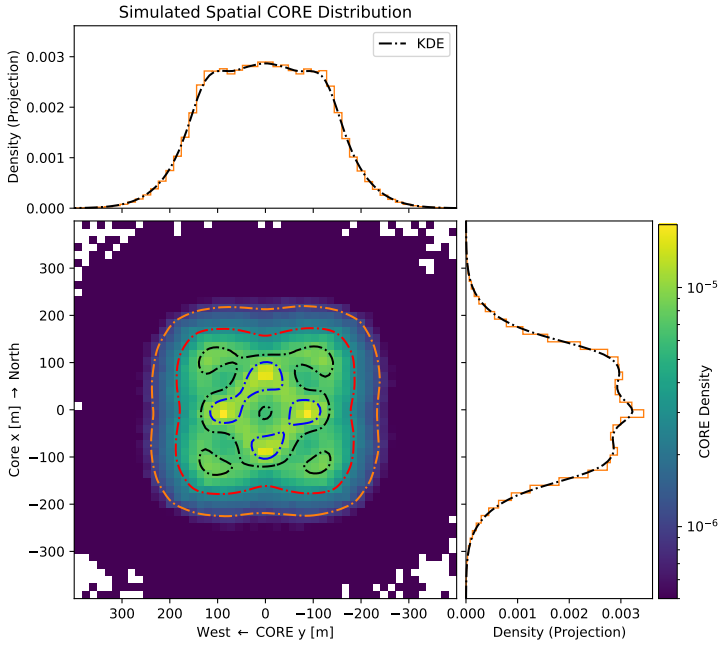

(b) CORE parameter distribution of simulated background events.

Figure 15: These two plots show the CORE distributions for the respective backgrounds. Besides of this, the plot's structure is comparable to Figure 9. The real distribution is more circular and blurred than the simulated one.

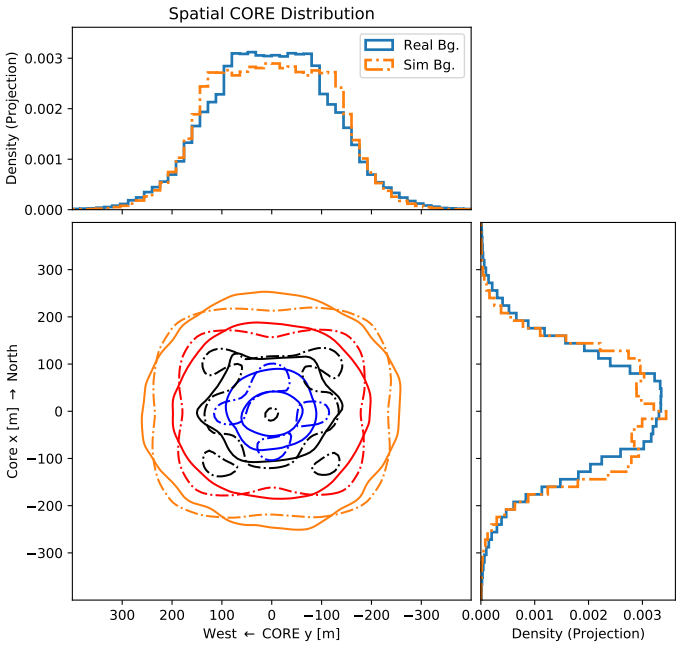

Figure 16: This plot shows the contour lines of the two CORE distributions in one plot. Whereas the real one is roughly circular, the simulated one is more square-like. The simulated distribution is more blurred than the simulated one.

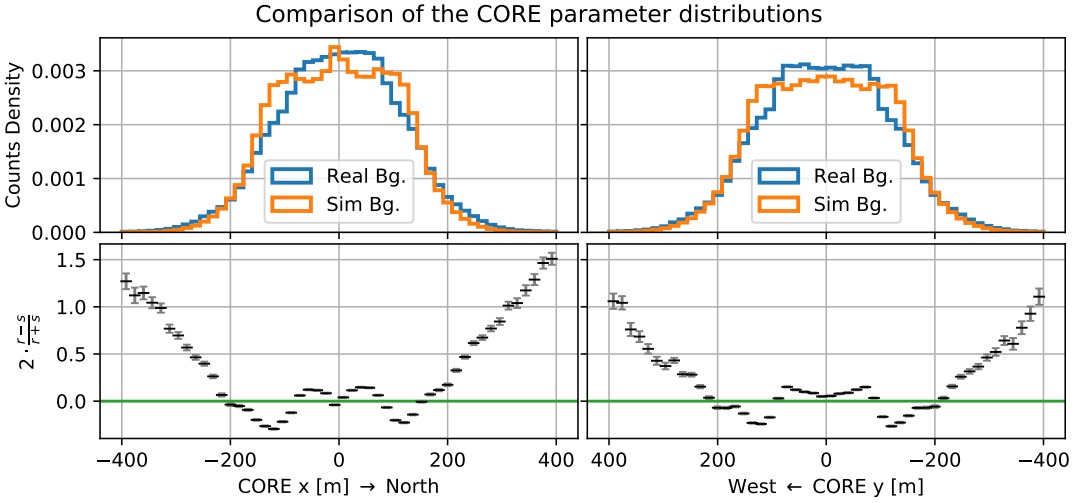

Figure 17: This plot shows the difference between the distribution in a more quantified way, using the comparison function described in subsection 2.3. One possible cause of these deviations could be differences in the multiplicity distributions of the two backgrounds.

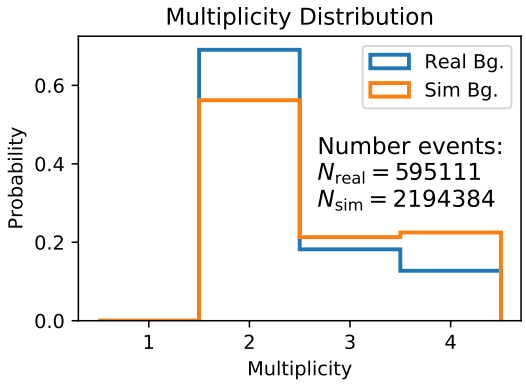

Figure 18: This plot shows the multiplicity distribution for the real and simulated background. An event's multiplicity describes the number of telescopes triggered by this event. The deviations could be caused by a faulty simulation of the telescope's dead times.

2.5 Multiplicity Distributions

In order to investigate the differences between the real and simulated CORE distribution, a histogram of the occurring multiplicities is shown in Figure 18. For this, events from phase 1b/d observations without known gamma sources in their FoV were used. The real background has more events with a multiplicity of two, whereas in the simulation favours a multiplicity of four. One probable reason for this difference is the dead time of each telescope. The dead-time describes the time duration after triggering, in which a telescope cannot detect new events. An inaccurate reproduction of these dead times could cause the seen deviations. However, the effect of these deviation can be counteracted by introducing some weights w_i:

$$p_{\text{sim}}(i) \cdot w_i = p_{\text{real}}(i) \tag{9}$$

Here, p(i) describes the probability of an event to have the multiplicity i, respectively either for simulated or real background events. The corresponding values can be found in the following table. The uncertainties were calculated by using a Poisson uncertainty.

Multiplicity	p_{real}	p_{sim}	w
2	$(69.07 \pm 0.11)\,\%$	$(56.21 \pm 0.05)\,\%$	1.2287 ± 0.0022
3	$(18.20 \pm 0.06)\,\%$	$(21.30 \pm 0.03)\,\%$	0.8543 ± 0.0029
4	$(12.73 \pm 0.05)\,\%$	$(22.49 \pm 0.03)\,\%$	0.5663 ± 0.0022

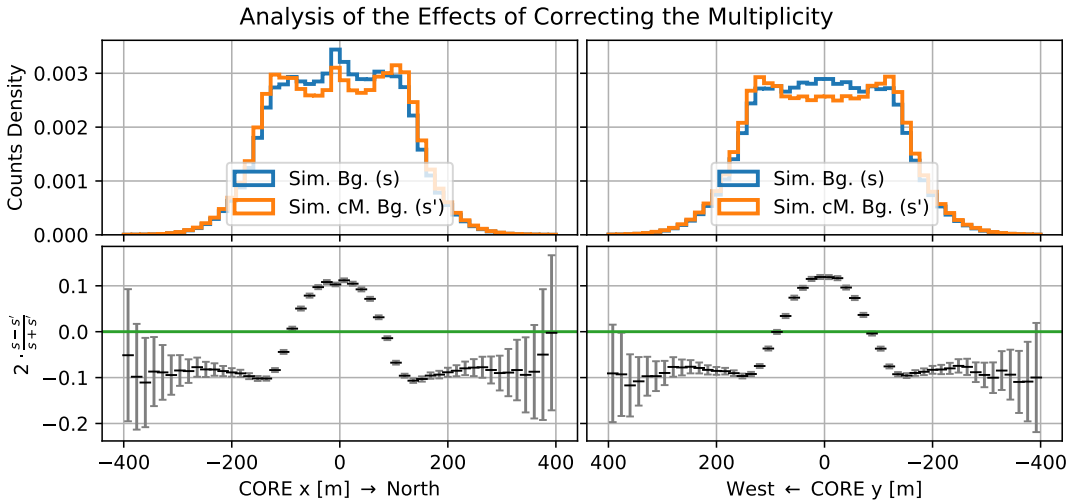

Figure 19: Resulting change of the CORE distribution after correcting the multiplicity. Figure 17 showed that the distribution of the simulated background is already too low in the centre FoV region. This deviation is now amplified by correcting the multiplicity distribution.

2.6 CORE distribution with adapted Multiplicity

The weights calculated above can now be used to align the simulated with the real multiplicity. This is done by using weighted histograms. The resulting change of the CORE distribution can be seen in Figure 19. It can be observed, that adapting the simulated multiplicity decreases the CORE distribution in the centre region, whereas the distribution increases in the FoV's edge regions. This is expected, as the calculated weights suppress the influence of events with a multiplicity of four, which are mainly located in the centre region. By introducing this multiplicity correction, the simulated CORE distribution decreases in the order of 10 %. However, Figure 17 shows that the simulation is, compared to the real background, even without the corrected multiplicity too low. As a result, the multiplicity adaption worsens the agreement of the CORE parameter between the simulated and real background.

Besides this, correcting the multiplicity should also influence the FoV distribution of the background model. A comparison between the FoV distribution of the unchanged and corrected multiplicity background can be seen in Figure 20. The correction of the multiplicity reduces the count distribution in the centre FoV region. This increases the deviations between simulated and real background model.

As shown in subsection 2.3, the deviations over the whole energy range are mainly influenced by the lowest energy bin, as this bin contains most of the observed events. Therefore, it is reasonable to analyse the effects of correcting the multiplicity for different

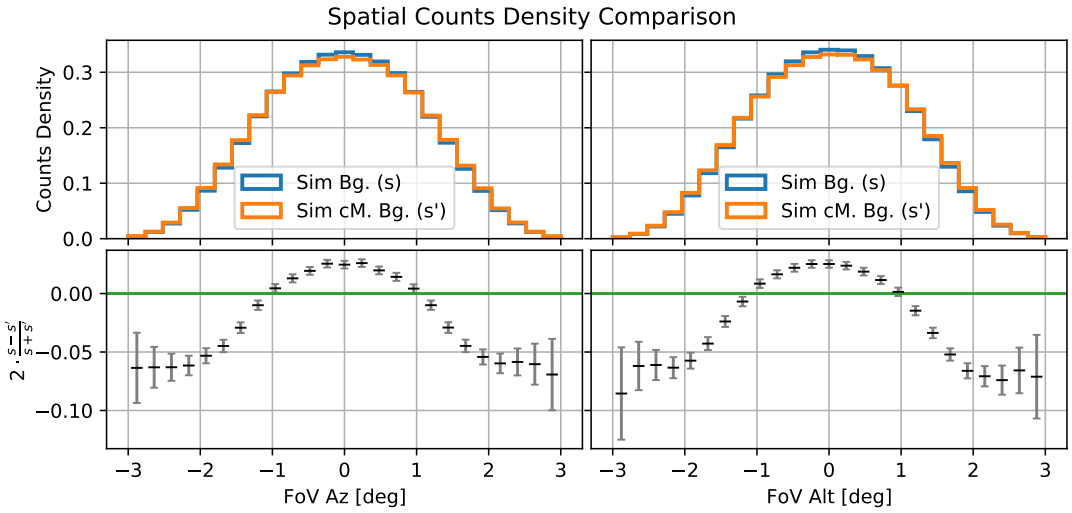

Figure 20: Showing the effects of correcting the multiplicity on the FoV event distribution. As for the CORE distribution in Figure 19, the correction of the multiplicity increases the overall deviations between simulated and real background.

energy bins. This is shown in Figure 21. In this plot, the vertical line of each marker depicts the uncertainty of the respective data point. As assumed, the correction of the multiplicity worsens the agreement between simulated and real background for the first energy bin. However, the second energy bin profits significantly from the corrected multiplicity. The mean deviation between the corrected multiplicity simulation s' and the real background r over the whole energy range is shown in the following table by averaging over the absolute values of the comparison function $d = 2 \cdot \frac{r-s'}{r+s'}$:

	$R = 1.0°$	$R = 1.5°$	$R = 2.0°$	$R = 3.0°$
FoV azimuth:	$(3.67 \pm 0.10)\,\%$	$(3.48 \pm 0.15)\,\%$	$(5.80 \pm 0.17)\,\%$	$(9.3 \pm 0.3)\,\%$
FoV altitude:	$(3.67 \pm 0.10)\,\%$	$(3.84 \pm 0.15)\,\%$	$(6.48 \pm 0.17)\,\%$	$(11.6 \pm 0.4)\,\%$

These mean deviations are continuously higher than this of the unchanged multiplicity simulation shown in Table 1. Following the behaviour of the overall agreement, it was decided to disregard the multiplicity correction for a later background model construction for now. In a second step, the correction of the multiplicity can be a possibility to improve the background model. In the optimal case, the parameter of the simulated H.E.S.S telescopes should be improved, so that the multiplicity correction is no longer required. This concerns in the first order the dead-times and optical efficiencies of the telescopes. If this is not possible, it can also be attempted to correct the multiplicity of the simulation only for a specific energy range, for example for energies above 0.68 TeV.

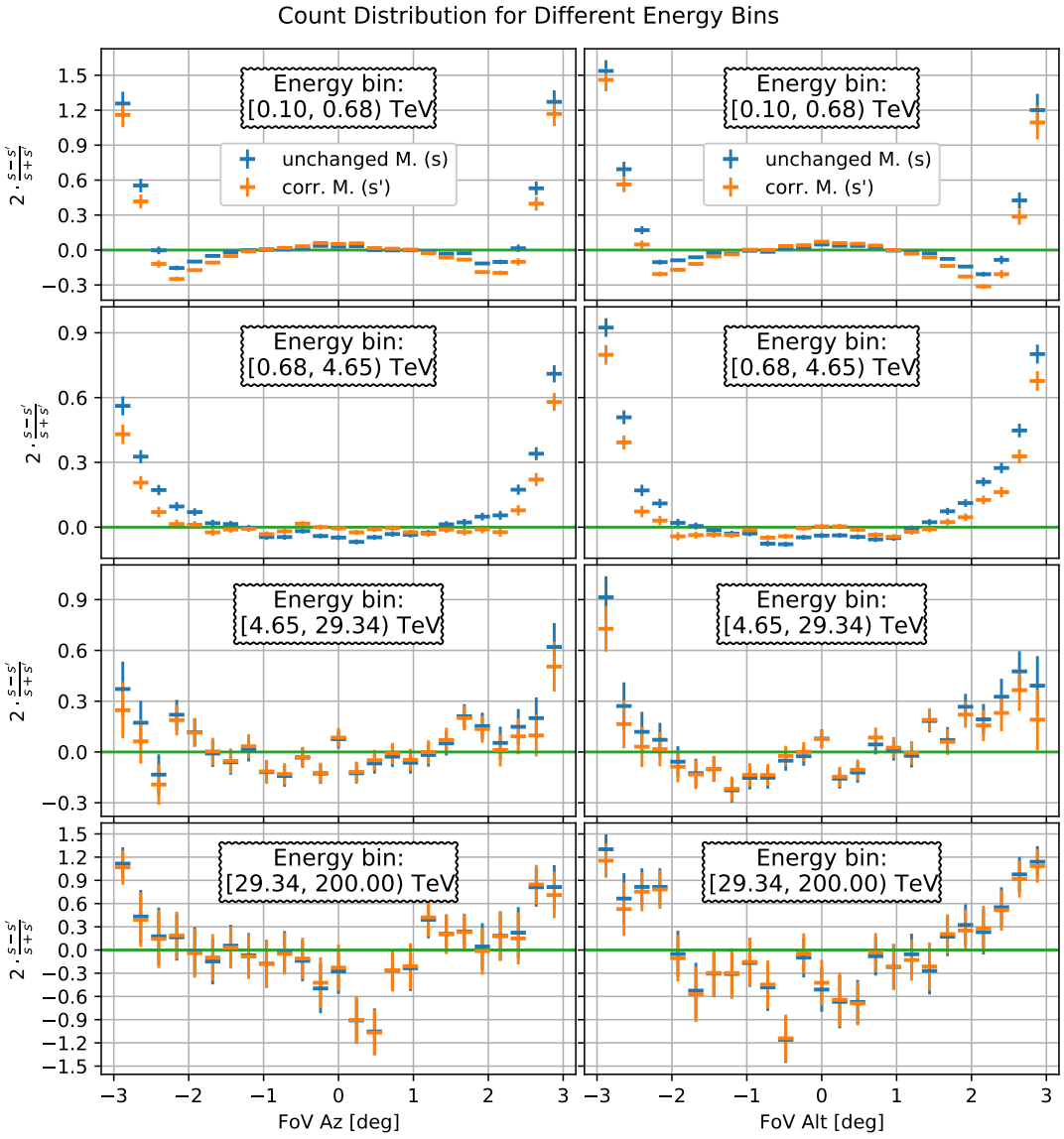

Figure 21: Deviations between simulated and real background for the unchanged simulation and for the corrected multiplicity simulation. As assumed before, the correction of the multiplicity worsens the agreement between simulated and real background in the first energy bin. However, especially the second energy bin from 0.68 TeV to 4.65 TeV profits significantly from the correction.

3 Using the Simulated Background to Analyse PKS 2155-304

In the last section, it was shown that the mean deviation between the simulated and real background in the centre FoV region ($R = 1.5°$) is $(2.10 \pm 0.09)\,\%$ in azimuth and $(2.16 \pm 0.11)\,\%$ in altitude direction. However, no salient way of decreasing these deviations were found. Yet, it is not clear how those deviations will influence later analysis results. One way of estimating this influence is to conduct analyses of a source, one using the simulated and one using the real background model. This thesis uses the existing real background model generated by L. Mohrmann et al. [1] with the version number v05c. It uses a FoV radec coordinate system.

3.1 Generation of the Simulated Background Model

To use the simulated background for a later analysis, a background model has to be generated at first. For this, all simulated observations were used. As the background model will describe the background rate, a live time duration is needed for each observation. For simulations, this information is missing. As a typical real observation covers around 30 min, it was also set to this value. This arbitrary choice of the duration can be compensated by fitting the resulting background model to each observation. Amongst others, this fitting process introduces a norm, which is multiplied to each pixel's predicted background count number, counterbalancing the set exposure time of the simulated observation. However, the set exposure value of 30 min is in the right order of magnitude: A mean real observation has a background count rate of 2 events per second.

For the background model, both of the two spatial FoV axes are divided into 50 bins with an overall width of 5°. The energy range of the model is set to 100 GeV to 100 TeV, using 24 bins per decade. However, the bin edges are adjusted in this way, that all BDT bin boundaries are also background model bin edges. Then, the number of simulated events in each resulting 3D bin is counted and stored to a FITS file. This general background template is then valid for all phase 1b observations with $15° \leq \text{zen} \leq 25°$ and $90° \leq \text{az} \leq 270$.

Afterwards, this general template must be extracted for each observation, for which the background should be estimated. Following the procedure for the real backgrounds, the energy axis is then rebinned to a coarser 34 bin segmentation. This is done to reduce statistical uncertainties of each bin's count rate. These fluctuations are then further reduced by smoothing over the bins' background rates. This is done by using a KDE. The resulting 3D background rate is then stored in a FITS file using a FoV altaz coordinate system. This file can then be read in for a later analysis. Apart from the specific binning, a similar process was used in subsection 2.2 and 2.3. Therefore, the made comparison between real and simulated background is also valid for these generated background models.

3.2 Description of the Fitting Process and the Source Significance Calculation

As mentioned before, the goal of this section is to compare the influence of the deviations between real and simulated background model onto a realistic analysis of a source. For the beginning, the source PKS 2155-304 was chosen, as it is a strong, well-known point-like source. One disadvantage of this source is, that it has an irregular flux variability between 10 % and 60 % of the crab flux [20]. However, as both analyses use the same set of observations, this variability is not relevant for the comparison between them. For PKS 2155-304, 86 observations with a combined live time of 41.2 h are available in the optical phases 1b/1d.

In this thesis, all analyses were done using Gammapy 0.18.2 [21], [22]. Gammapy is one of two candidates to become the standard high-level analysis tool for the next generation gamma observatory, the Cherenkov Telescope Array (CTA). The package is based on Numpy [23], Scipy [24] and Astropy [25], [26]. It is able to perform a binned, 3D, energy-resolved likelihood analysis. In this analysis, one can use different model components to describe the observed data. For PKS 2155-304, the following components will be used:

1. Background: The observed background of the observations shall be described by background model templates. The functionality of background templates was described in subsection 1.5.3. In this section, two analyses are conducted: One time with the standard background model, generated using real observations. The other time the simulated background model is used, its generation was described in subsection 3.1.
2. Spatial shape of the source: The spatial shape of PKS 2155-304 is assumed to be point-like. Therefore, Gammapy's Point Spatial Model is used. It distributes the predicted counts onto four neighbouring pixels in that way, that the centre of mass position is conserved. In combination with the Instrument Response Function (IRF), the resulting instrument behaviour can be predicted.
3. Energy spectrum of the source: For PKS 2155-304, reasonable assumptions could be a Power Law, an Exponential Cut-off Power-law or a Log Parabola spectral model (For definitions, see Table 2). Recent publications suggest that a Log Parabola model is most suitable. Nevertheless, to keep the fitting process and the following comparison simple, a plain Power Law model was chosen.

3.2.1 Theory using Cash Statistic

For the fitting process, it is assumed that the measured counts n_i in each bin i are Poisson distributed:

$$P_m(n) = \frac{m^n}{n!} \cdot \exp(-m) \tag{10}$$

	Power Law	Exponential Cutoff Power-law	Log Parabola
Def.:	$\phi = \phi_0 \left(\frac{E}{E_0}\right)^{-\Gamma}$	$\phi = \phi_0 \left(\frac{E}{E_0}\right)^{-\Gamma} \exp -(\lambda E)^{\alpha}$	$\phi = \phi_0 \left(\frac{E}{E_0}\right)^{-\alpha-\beta\log\left(\frac{E}{E_0}\right)}$

Table 2: Definitions of different energy spectra models [27]. It was decided to use the Power Law model for PKS 2155-304, as it simplifies the fitting process and the later comparison, while still modelling the source in an acceptable way.

Here, m_i is the expectation value for the bin i, in this case predicted by the respective model. The combined log likelihood of all pixels is then:

$$\log(\mathcal{L}) = \log\left(\prod_{i=1}^{N} \frac{m_i^{n_i}}{n_i!} \cdot \exp\left(-m_i\right)\right) = \sum_{i=1}^{N} \left(n_i \cdot \log(m_i) - \log(n_i!) - m_i\right) \tag{11}$$

This equation uses the natural logarithm and the number of pixels N. By multiplying this equation by -2 and by dropping the term $-\log(n_i!)$ one gets the so-called cash statistic:

$$C = 2\sum_{i=1}^{N}(m_i - n_i \log(m_i)) \tag{12}$$

By minimising the cash statistic C, the best fitting parameters for a given model m can be found. That technique was proposed by and named after Webster Cash [28].

It can be combined with the fundamental theory of Wilks [29]: If m' is nested into m, meaning that $m = m'$ if q parameters of m are held constant at their true values, then [28]:

$$\Delta\mathrm{TS} \coloneqq -2\log\left(\frac{\mathcal{L}(m')}{\mathcal{L}(m)}\right) \text{ is distributed as } \chi^2_q + \mathcal{O}\left(\frac{1}{\sqrt{N}}\right) \tag{13}$$

If the cash statistic is used, ΔTS can also be written as

$$\Delta\mathrm{TS} = C(n, m') - C(n, m) \tag{14}$$

In astronomy, this can be used to estimate the significance of possible source. For this, one assumes that m is the combined background and source model, whereas in m', the amplitude of the source is set to 0. Consequently, m' is a nested into m and q is one. In this special case, m is preferred over m' with a significance value of $\sqrt{\mathrm{TS}}$. This is then the significance of the source candidate.

3.2.2 Resulting parameters

Before the fitting is started, the so-called energy bias of IACT telescopes has to be considered: This describes the effect, that for events with a true energy near the telescope's minimum energy, events with larger air showers are more probable to be detected than these with smaller ones. As an events air shower size is randomly distributed

around one mean value, this leads to a bias in the reconstruction of the events' true energy. This can be prevented by using a safe energy threshold. It was chosen to limit this energy bias to 10 %. Additionally, the usage of a background template model imposes the need of an own energy threshold, as described in [1]. For this, the upper edge of the energy bin with the highest predicted background rate is used. For each observation, these two requirements result into one energy threshold, defined as the maximum of the energy bias and background threshold. To make the different observations comparable, the highest observed energy threshold was used for every observation. For the selected PKS 2155-304 observations, this threshold is at 0.422 TeV. The resulting energy analysis range is then 0.422 TeV to 100 TeV, using eight bin per decade. The common spatial coordinate system has a width of $5° \times 5°$, using 250×250 spatial bins. Every spatial bin covers then an area of $0.02° \times 0.02°$. As proposed before, only events within a radius of 1.5° around the respective FoV centre were used for the analysis.

As the first step, the background model is adjusted to every observation separately. This adjustment is done by multiplying the following model to the predicted background rate R_{bg}:

$$R'_{\mathrm{bg}} = R_{\mathrm{bg}} \cdot \mathrm{norm} \left(\frac{E}{E_0} \right)^{-1 \cdot \mathrm{tilt}} \tag{15}$$

After excluding a region with a distance to the source position of less than 0.3°, the model's parameters tilt and norm are found by fitting R'_{bg} to the remaining data. Here and following, the reference energy E_0 is set to 0 TeV. This observation-based fitting process should counteract the influence of varying atmospheric conditions. The resulting parameter distribution is shown in Figure 22. In this plot, the vertical lines are marking the mean of the respective distribution. A deviation mean value is not problematic, as both the exposure time and the spectral index of the simulated background counts were chosen manually. However, the variance σ^2 and the connected standard deviation σ should be similar. This is true for the tilt parameter, but not for the norm distribution. One possible explanation could be, that the fit is less stable for the simulated background analysis. However, the distribution of the uncertainties calculated by the fits are similar: 0.045 ± 0.005 for the standard and 0.044 ± 0.005 for the simulated background analysis.

These single fits are then stacked, building a single background model able to model the combined background of all observations. Although theoretically not necessary, the combined background model can then again be adjusted to the measured data. Now, the source region is not excluded, but rather modelled by the source model. This should result in a tilt value of 0 and a norm value of 1. Deviations of this value would show, that either the first fitting step was not successful, or that there are severe problems with the source model. The resulting parameters of this fitting process can be seen in Table 3. The parameter of the analyses using the simulated and real background are in agreement with another. In principle, the slightly increased norm value could indicate that the source model's counts prediction is too low. The lower Cash statistic C of the model generated by using the standard background shows, that its predictions are fitting better to the real measured data than that of the model using the simulated background.

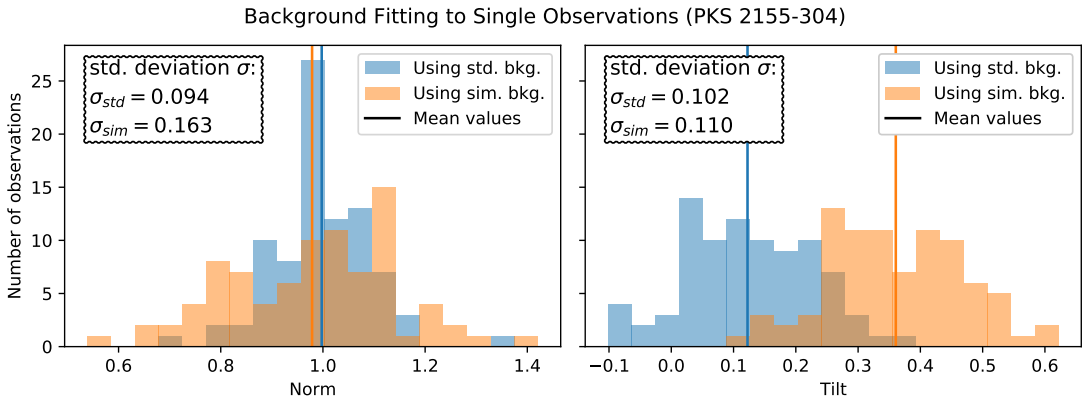

Figure 22: This plot shows the parameter distribution of the background fitting to the separate observations. Different mean values are expected, as the exposure and the simulated spectral index were manually chosen. However, the variance σ^2 of the distributions should be similar. This is true for the tilt distributions, however, the norm standard deviations σ are deviating, possibly caused by a less stable fit.

	Parameter	Value		Unit
		Using real background	Using simulated bkg.	
Source	Index Γ	4.13 ± 0.05	4.15 ± 0.05	
	Amplitude ϕ_0	$(4.84 \pm 0.19) \times 10^{-12}$	$(4.76 \pm 0.19) \times 10^{-12}$	$\mathrm{cm}^{-2}\mathrm{s}^{-1}\mathrm{TeV}^{-1}$
	Ra	329.7180 ± 0.0010	329.7179 ± 0.0011	°
	Dec	-30.2221 ± 0.0009	-30.2221 ± 0.0009	°
Bkg	Norm	1.005 ± 0.005	1.004 ± 0.005	
	Tilt	0.006 ± 0.007	-0.006 ± 0.008	
Cash statistic C		201 379	201 943	

Table 3: This table shows the fitted parameter for the source PKS 2155-304, one time for the real, the other time for the simulated background. It can be seen that the simulated and real background's parameters are in agreement with another. The largest deviations can be seen for the tilt parameter, but also here the deviations are below 2σ. The lower Cash statistic of the analysis using the real background indicates, compared to the analysis with the simulated background, a better overall agreement between reality and fitted model.

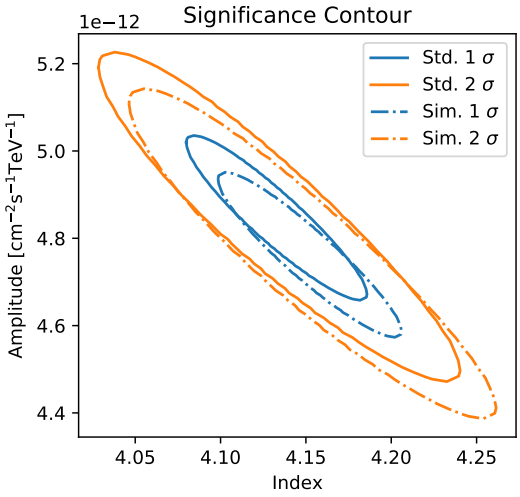

Figure 23: This plot shows the confidence contour for the amplitude phi_0 and index Γ of the two source models. The two parameters are in both analyses correlated. The analyses' results are in agreement with one another.

One point not described by this table is the parameters' correlation with one another. Mainly, this concerns the index and amplitude parameters of the source models. This correlation can be made visible by using a confidence contour plot, as shown in Figure 23. In this plot, a $n\sigma$ contour line encloses the area, where the log likelihood is less then $n\sigma$ above the minimum. For two uncorrelated variables, the main axis of the generated ellipse would be either horizontal or vertical (depending on the axes' scaling). The plot confirms the statement from before, that the parameters from the simulated and real background analysis agree with one another.

The combination of the PKS 2155-304 source model with the background model should now describe all measured counts. This enables to show the spatial distribution of the modelled source and background counts, as shown in Figure 26. Compared to the background, the source is strong and clearly recognisable.

As described in the previous section, the significance of the source can be calculated by conducting an additional fit without the model's source components. The resulting parameters can be found in Table 6. The ΔTS values correspond to a source significance of 130.2σ for the real and 129.5σ for the simulated background. These significance values are comparable.

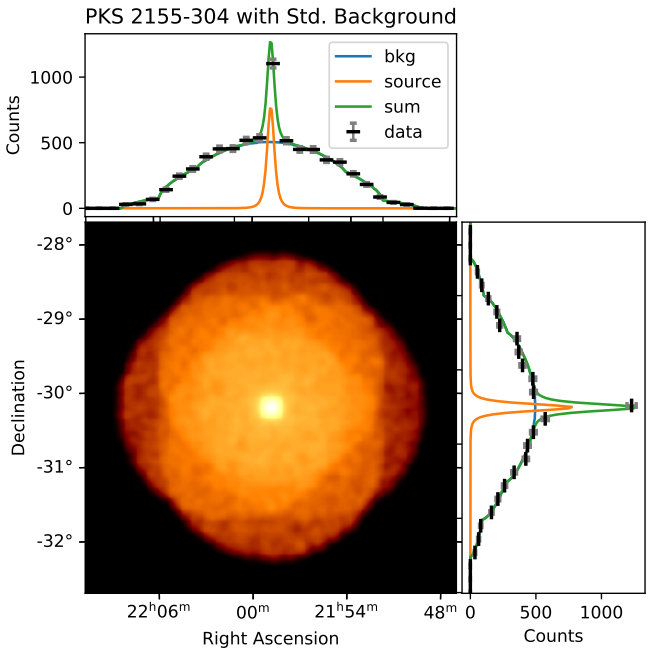

Figure (25) Counts distribution in combination with the fitted source and background model of the standard background analysis.

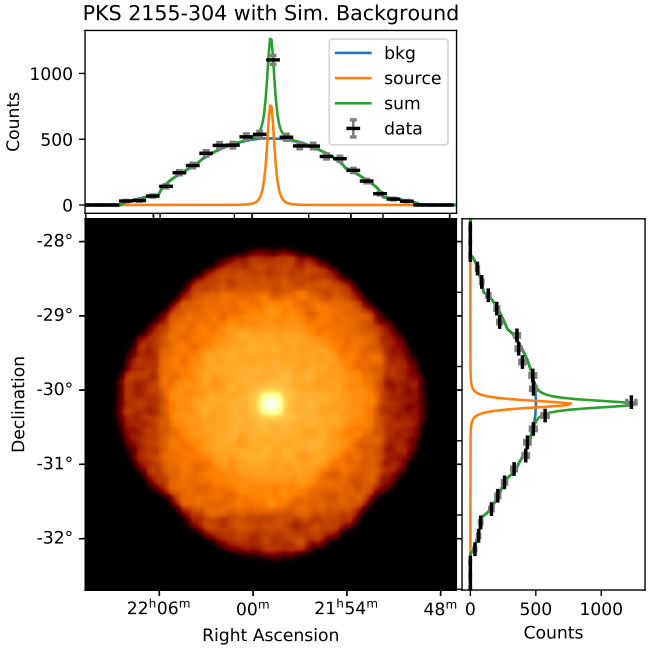

Figure (26) Counts distribution in combination with the fitted source and background model of the simulated background analysis.

Figure 26: The four superimposed circles in the main plot indicate that the observations were taken in wobble mode. The smaller plots show the fitted source and background models, summed over one spatial axis. For improved readability, only every ninth data point combined with a Poisson's uncertainty was plotted. Compared to the background, the source is clearly recognisable.

Parameter	Value	
	Using real background	Using simulated bkg.
Norm	1.089 ± 0.005	1.086 ± 0.005
Tilt	0.039 ± 0.007	0.042 ± 0.007
Cash statistic C	218 338	218 719

Table 4: This are the relevant parameters, if the model's source components are omitted. As the background fit model is now influenced by the source, both the norm and the tilt are increased compared to the regular fit shown in Table 3.

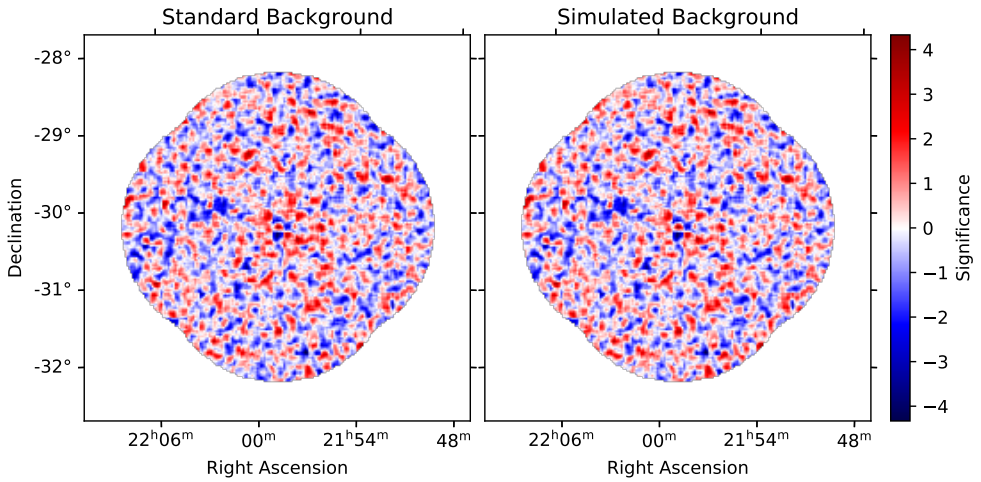

Figure 27: This plot shows a$\sqrt{\text{TS}}$ map of the standard and simulated background analysis. It gives the significance of an imaginary point source at each pixel using the respective background model and the fitted PKS 2155-304 source model. The point source is modelled to have a Power Law spectrum with an index of $\Gamma = 2.7$.

3.3 $\sqrt{\text{TS}}$ Maps and Significance Distributions

The calculation of the significance can not only be applied to the position of PKS 2155-304, but also to every other pixel position. For this calculation, the likelihood can be calculated by using the deviations between predicted (by source and background model) and measured counts. These deviations are called residuals: $r_i = n_i - m_i$. Negative residuals are indicated by making the resulting significance value negative. These residual significance values can then be used to visualise the residuals map, and with it the spatial consistency between measurement and prediction. Here, a probe point source model with an index of 2.7 is used. As of now, this procedure would convolve the point spatial model with the entire Point Spread Function (PSD), concealing possible small-scale deviations. This can be prevented by truncating the PSD, here to a width of 0.1°. The resulting plot is shown in Figure 27. It can be seen that the results generated by the simulated and real background analysis are very similar. This is an import comparison argument, as it emulates the search for gamma sources. This representation of the residuals can also be used to look for possible gradients. Although no clear gradient is visible, there is the impression that the centre region of both plots is tendentially too red.

Another test criteria strongly connected with this representation is the significance value distribution, referring to the probability density function of the single significance values. For a perfect source and background model, this should be a Gaussian distribution with mean value $\mu = 0$ and standard deviation of $\sigma = 1$. The fitting process aims to

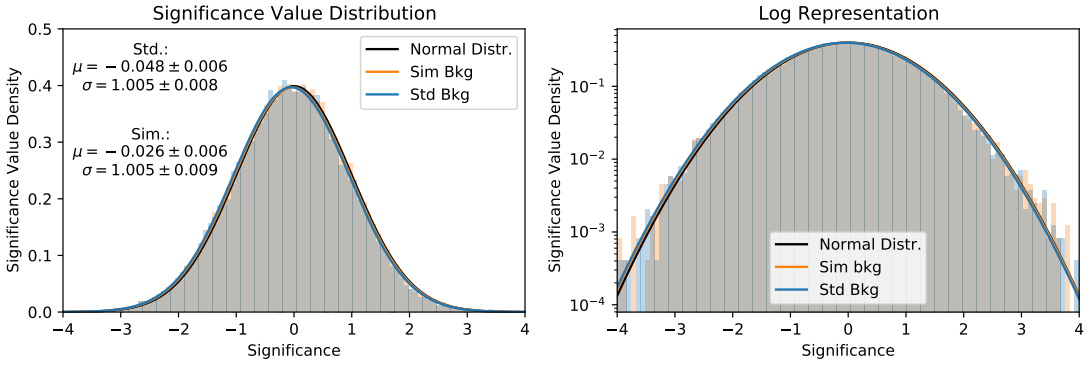

Figure 28: This figure shows the significance value distribution of the $\sqrt{\text{TS}}$ map. The Probability Density Functions (PDFs) of the simulated and standard background analysis are near the desired normal distribution.

attain a mean residual value of $\mu_r = 0$. For symmetric residual distributions, this is automatically resulting in a mean significance value of $\mu = 0$. However, asymmetrical residual distributions can cause small deviations from this target value. In contrast, large deviations indicate problems with the fitting process itself.

One probable reason for a deviation standard deviation would be a under- or overfitting. This means, that the used combination of source and background model is either too simple or too complex to correctly describe the measured data. For example, this can happen if there are undetected gamma sources, causing an increased standard deviation.

The calculated significance value distribution can be seen in Figure 28. The resulting mean and standard deviations of the two distributions are as expected. For the standard deviation, the desired value of 1 is for both analyses in the respective uncertainty range. This is not true for the mean value: Here, both the simulated and standard background analysis are deviating from the desired value of 0. In this case, the standard analysis' value is more off than the simulated one. However, both deviations are small and therefore acceptable for now. In general, this significance value distribution could also be plotted for different energy bins, as done for the FoV distributions in subsection 2.3. However, as counts can only be positive, the significance value distributions loos their Gaussian shape for low count numbers, as it is the case for larger energies.

Beyond this, one can use the significance value distribution to verify, if the centre FoV region is indeed showing, as suspected before, a surplus of positive significance values. For that, the significance value distribution can be calculated for the respective region, here for the area inside a circle with a radius of 0.3° around the source position. This is shown in Figure 29. One can see that the mean significance value is indeed increased, supporting the hypothesis of increases significance values in the centre region. Probable causes for this could be a bad source model or by a faulty PSD. Either way, the combined background and source model is then not complex enough, causing an increased standard

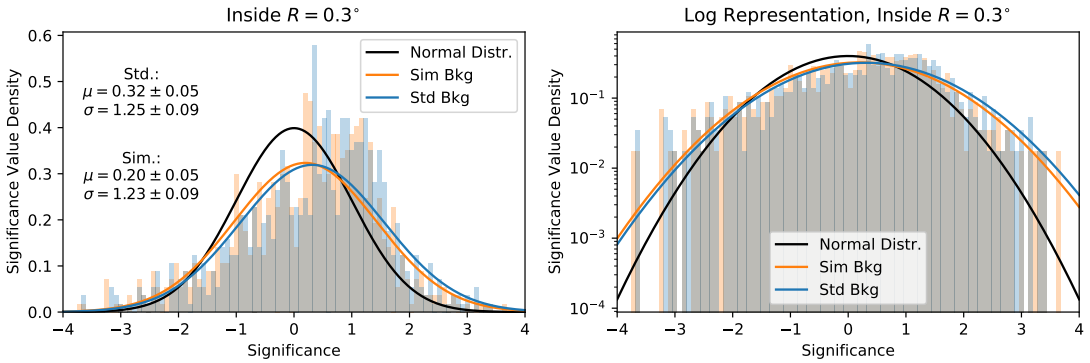

Figure 29: This plot shows the significance value distribution for the FoV region inside a circle with a radius of 0.3° deg around the source position. The increased mean value μ shows, that the model for this region is too low. This could be caused by a bad source model or an inaccurate PSD. Consequently, the combined source and background model is not complex enough, resulting in an increased standard deviation. For this region, the mean value of the simulated background analysis is nearer to the desired value of $\mu = 0$ than the standard analysis.

deviation. Overall, the performance of the simulated background analysis is here better than the standard one. As both analyses show this anomaly, a background model problem is implausible.

3.4 Energy Dependent Comparison between Model and Data

In the last subsection, significance maps were used to find spatial gradients. However, this covers only one part of possible deviations between the model and data. The other important part are the deviations along the energy axis. For this, the predictions of the combined source and background model for each energy bin are combined with the actual measured data, summed up over the entire FoV. For the data, a Poisson's uncertainty $\sqrt{N}$ was assumed. The result can be seen in Figure 30. For better visibility, the deviations d_i between the counts data and the respective model in units of statistical significances $\sigma_{i,\mathrm{stat}}$ is shown in the subplot below.

It can be observed that the deviation of the model using the standard background is lower than that of the simulated one. The larger deviations at lower energies can be explained by the small uncertainties caused by large counts numbers. In general, the RMS of the deviations in units of significances must be equal to one. As of now, the uncertainties are only caused by the statistical uncertainties, which were calculated using the Poisson distribution. This yields a RMS value of 3.899 for the standard and 6.649 for the simulated background analysis. This indicates that the statistical uncertainty alone is

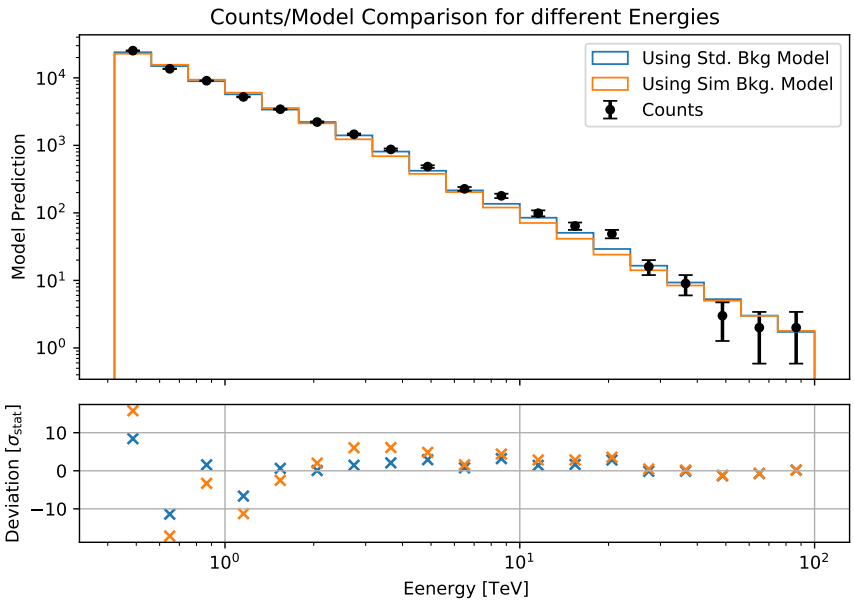

Figure 30: This plot shows the energy dependent deviations between the combined background and source model and the measured data. Here, the performance of the standard background fitting is superior.

not able to explain the observed deviations. Therefore, one can introduce a systematical uncertainty σ_{sys} using the assumption that it is proportional to the number of predicted counts m:

$$\sigma_{i,\text{sys}} = \delta_{\text{sys}} \cdot m_i \tag{16}$$

The combined uncertainty σ can then be calculated as following:

$$\sigma_i = \sqrt{\sigma_{i,\text{stat}}^2 + \sigma_{i,\text{sys}}^2} \tag{17}$$

The value of δ_{sys} can then be estimated by requiring that the RMS value of the observed deviations in units of the combined uncertainty σ is equal to 1. This approach was adopted from A. Specovius [30]. It yields a systematical error of 11.7 % for the standard and 26.7 % for the simulated background analysis model. The resulting deviation histograms can be seen in Figure 31. These two values show clearly that the analysis using the standard background can predict the observed counts better than the simulated one. However, both systematical uncertainties are substantial and must be considered when analysis results are interpreted.

3.5 Source Model and Flux Points

In the previous subsection it was shown that there are substantial differences between the prediction and the measured counts for different energy bins. One important factor is,

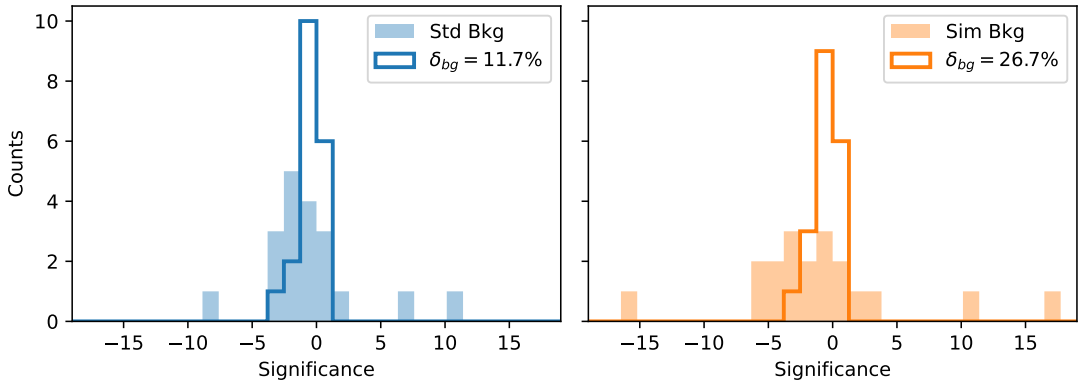

Figure 31: This figure shows two histograms of observed model/counts deviations, one time for the standard and one time for the simulated background analysis model. Each plot shows these deviations with and without the calculated systematical error.

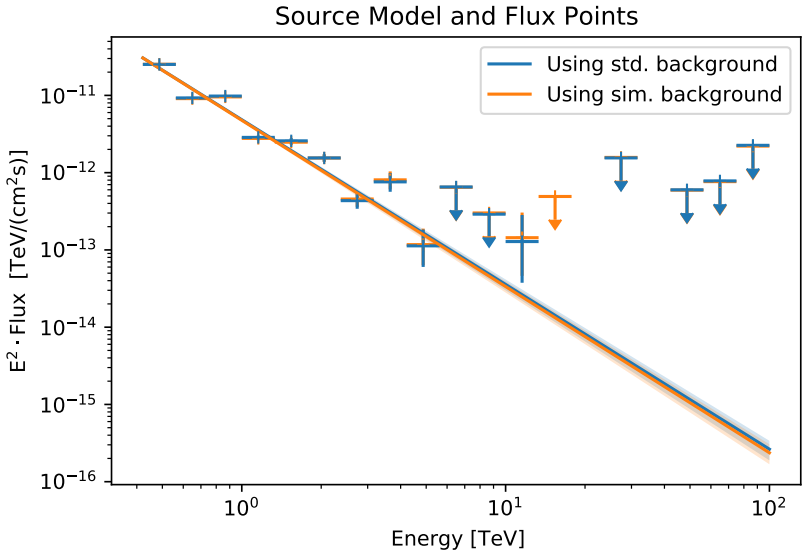

Figure 32: This plot shows the calculated flux points of the standard and simulated background analysis. The source model itself, here a power law model, is also shown. It can be seen that the flux points and source model of both analyses are very similar. The energy bins with missing data points are caused by negative flux points or upper limits.

how these differences influence the fitted source model. In general, already in subsection 3.2.2 it was shown that the fitted amplitude ϕ and index Γ of the two analyses are compatible with one another. A more detailed comparison can be conducted by using flux points. A flux point can be calculated by fitting the amplitude of the source model to data within the specific enenery bin. The associated uncertainty bands are calculated using the fit's TS profile. If an energy bin's source model has a significance of less than 2σ or predicts a negative amplitude, then an upper limit of 2σ is computed. This procedure of calculating flux points is also described in the H.E.S.S Galactic Plane Survey paper [18]. The calculated flux points, together with the best-fit source models, can be seen in Figure 32. The missing flux points for some energy bins are caused by negative flux points, which are not visible in this logarithmic plot. Flux points are getting negative, if the fitted amplitude of the source model is negative, resulting from a too high predicted background. Overall, the flux points and the resulting power law model for the two analyses are very similar.

In conclusion, for PKS 2155-304, it was observed that the analysis using the standard background model yields a better agreement with the measured data than the analysis using the simulated model. However, it was shown that both models have a substantial systematic uncertainty which cannot be neglected. Looking at the results of the analyses, it can be seen that the found parameters of both analyses are very similar, for example as shown in Figure 23. Albeit, it must be considered that PKS 2155-304 is a strong gamma source. For this reason, an analysis of Centaurus A (Cen A) is conducted in the following section. This is a weaker point source, which is expected to increase the influence of the background model on the analysis.

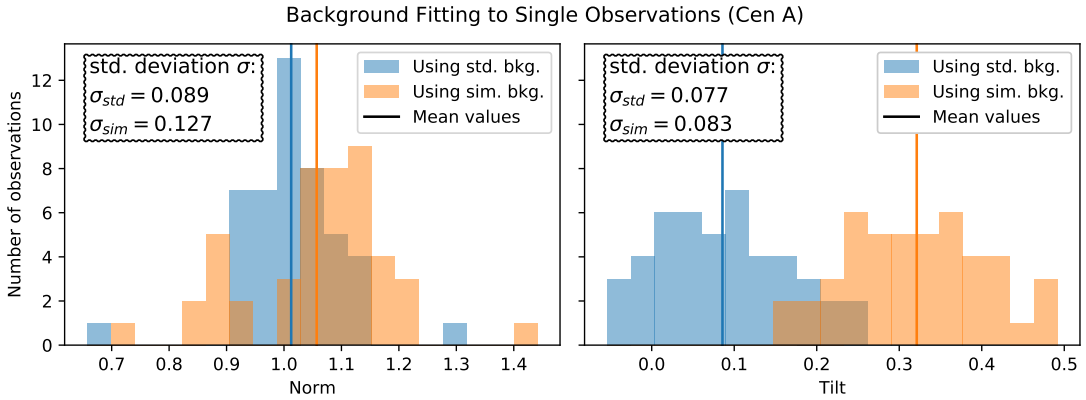

Figure 33: This plot shows the parameter distribution for the single background adjustments. The interpretation is of this plot is equal to that of Figure 22.

4 Analysis of Centaurus A

Up to now, the simulated background model was only used to analyse a strong gamma source. However, the analysis of weak sources is more difficult, as in this case an inaccurate background model is expected to have a stronger influence on the analysis results. In this section, the performance of the simulated background model described in subsection 3.1 is evaluated. For this, the radio galaxy Centaurus A (Cen A), a weak gamma source, was chosen. In a reasonable energy range of 0.4 TeV to 100 TeV, the number of detectable events is expected to be around 15 times smaller than for PKS 2155-304 [31], [32].

In this section, an analysis of Cen A using the simulated background model is compared to one using the standard background model. Both background models were described earlier in section 3. If not noted otherwise, the procedure of this section is the same as for PKS 2155-304 in section 3. For Cen A, 46 phase 1b observations in the suitable zenith/azimuth bin of $15° \leq \text{zen} < 25°$ and $90° \leq \text{az} < 270°$ are available, corresponding to a combined observation time of 21.5 h. Phase 1d did not contain suitable observations. The used safe energy threshold for these observation is 0.422 TeV.

As for pks, it was decided to model Cen A by assuming it to be point-like (Point Spatial Model) with a power law spectrum. According to Abdalla et al. from 2018 [32], these assumptions are justified. The parameter distribution of the background fits to the single observations can be seen in Figure 33. These distributions are similar to the ones of PKS 2155-304 in Figure 22, resulting into the same interpretation.

The results of the subsequent background and source model fits can be found in Table 5. As for PKS 2155-304, the two parameter sets (one using the standard, one the simulated background model) are comparable. However, due to the small combined exposure time and the weak gamma source, the uncertainty bands are large. As before, the slightly

	Parameter	Value		Unit
		Using standard bkg.	Using simulated bkg.	
Source	Index Γ	2.8 ± 0.4	2.7 ± 0.5	
	Amplitude ϕ_0	$(1.8 \pm 0.6) \times 10^{-13}$	$(1.7 \pm 0.6) \times 10^{-13}$	$\mathrm{cm}^{-2}\mathrm{s}^{-1}\mathrm{TeV}^{-1}$
	Ra	201.381 ± 0.015	201.379 ± 0.008	$^\circ$
	Dec	-42.997 ± 0.017	-42.995 ± 0.019	$^\circ$
Bkg.	Norm	1.0025 ± 0.0061	1.0016 ± 0.0062	
	Tilt	0.0005 ± 0.0097	0.0012 ± 0.0100	
Cash statistic C		166709.4	166900.0	

Table 5: This table shows the found parameters of the two Cen A analyses, one using the standard and one using the simulated background model. Both parameter sets are comparable. Due to a low observation time and the weak source, the uncertainty bands are large.

Parameter	Value	
	Using real background	Using simulated bkg.
Norm	1.0043 ± 0.0061	1.0032 ± 0.0061
Tilt	0.0000 ± 0.0096	0.0006 ± 0.0100
Cash statistic C	166 722.5	166 911.1

Table 6: This are the relevant parameters, if the model's source components are omitted. As the background fit model is now influenced by the source, the norm is now increased compared to the regular fit shown in Table 3.

increased norm value could indicate a too small counts prediction of the source model, possibly caused by a too narrow point spread function. The lower cash statistic of the standard background analysis shows that its model is fitting the measurements more precisely.

The corresponding significance contour of the amplitude ϕ_0 and the spectral index Γ is shown in Figure 34. For Cen A, the two parameters are less correlated as for PKS 2155-304. Noticeable is, that for low amplitudes a wide range of spectral indices has a similar likelihood value. This effect could be caused by the low significance value of the source. Overall, the shapes of the two contours are similar, albeit small shifts between the two contours are visible.

To calculate the significance of the source, the background model is once again fitted to the combined observations, but this time without the source model. The resulting parameters are shown in In order to improve the comparability between the two tables, the norm and tilt parameters were rounded in both tables one digit later. The differences between the Cash statistics C correspond to a source significance of 3.61 for the standard and 3.33 for the simulated background analysis.

This small significance is also visible in Figure 35: The source is only visible, as the

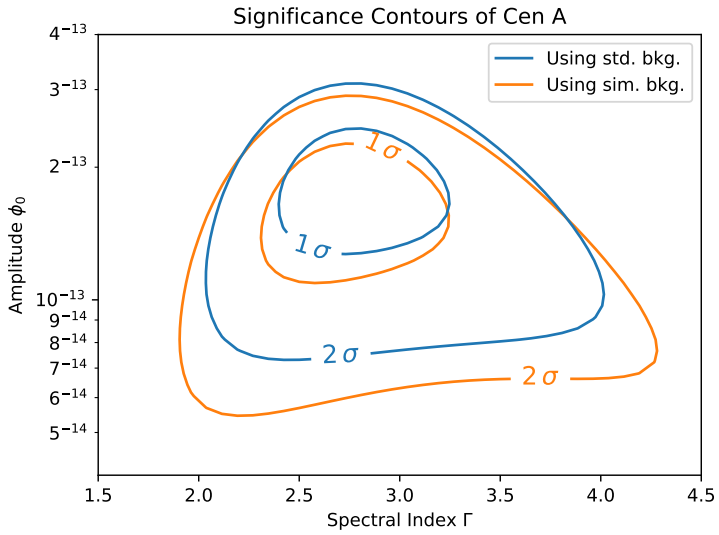

Figure 34: Confidence contours of the amplitude ϕ_0 and spectral index Γ parameter of Cen A. Both shape are similar and only small deviations are visible.

summation for the two smaller plot was limited onto the range between the respective two blue lines. This, in combination with the smaller overall observation time, is causing larger uncertainties of the data points.

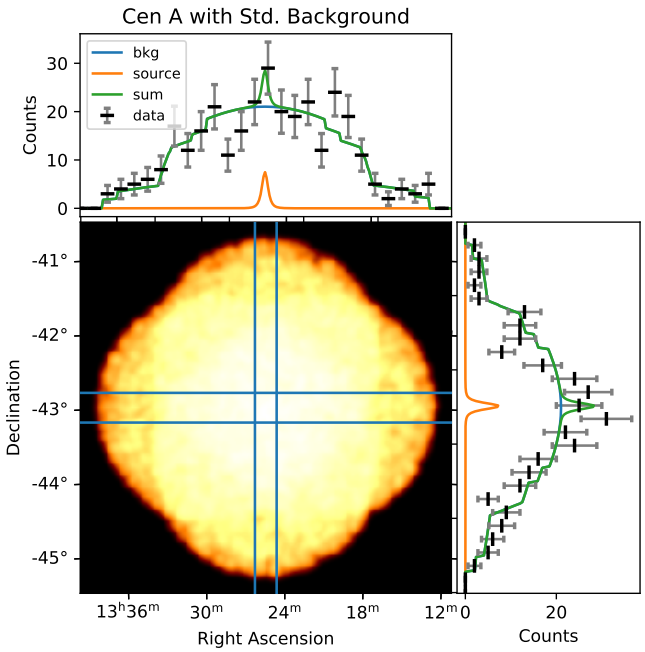

(a) Counts distribution in combination with the fitted source and background model of the standard background analysis.

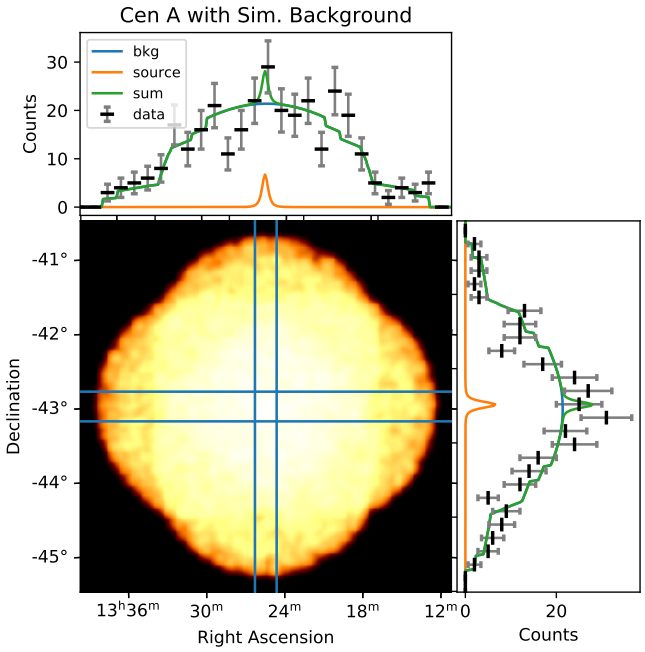

(b) Counts distribution in combination with the fitted source and background model of the simulated background analysis.

Figure 35: The main plots show the counts distribution of the selected observations. The smaller plots show the measured counts and the fitted source and background models, summed up between the two blue lines. The source is only visible because the summation was limited onto the region between the two blue lines. For improved readability, only every ninth data point combined with a Poisson's uncertainty was plotted.

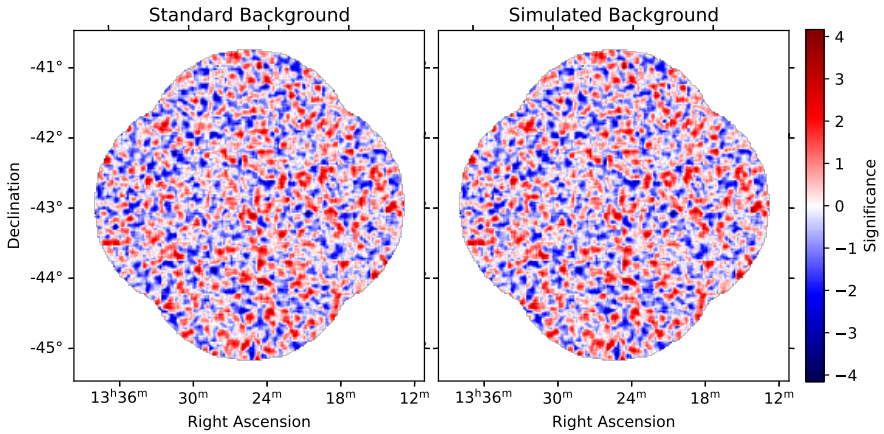

Figure 36: Spacial $\sqrt{\Delta TS}$ Map for Cen A. The source model was truncated to a width of 0.1° to show also small details. This truncation increases the fitted significance values. No obvious gradients are visible.

4.1 $\sqrt{\Delta TS}$ Maps and Significance Distributions

Figure 36 shows the spatial $\sqrt{\Delta TS}$ map for Cen A. It shows the significance of an imaginary point source with spectral index of $\Gamma = 2.7$ at each spatial pixel. A detailed description can be found in subsection 3.3. In order to increase the visible details of the map, the test source model was truncated to a width of 0.1°. In general, such a truncation leads to higher observed significance values, as the truncated source model uses less area. However, this plot would show possible gradients in the FoV, but none are visible. The corresponding significance value distribution is unremarkable, it is shown in Figure 37. As for PKS 2155-304, the mean values of the distributions are negative. The standard deviations are slightly increased, but both distributions have the same value.

As mentioned, Cen A is a considerably weaker gamma source than PKS 2155-304. This can be used further analyse the observed FoV edge to centre gradient, observed in subsection 3.3: If this gradient is indeed caused by a bad source model, then a weaker gamma source in combination with a unchanged background model would lead the a less pronounced effect, assuming that the residuals of the source model are somehow proportional to the amplitude of the source. The gradient can be estimated by plotting the significance value distribution for pixels of the centre region, as shown in Figure 38. However, the effect of an increased mean value for the centre FoV area is here even more distinct: For the standard background model, this value increased from 0.32 ± 0.05 for PKS 2155-304 to 0.36 ± 0.04 and for the simulated background model from 0.20 ± 0.05 to 0.27 ± 0.04. This makes it probable, that the increased mean significance is not caused by a faulty source model.

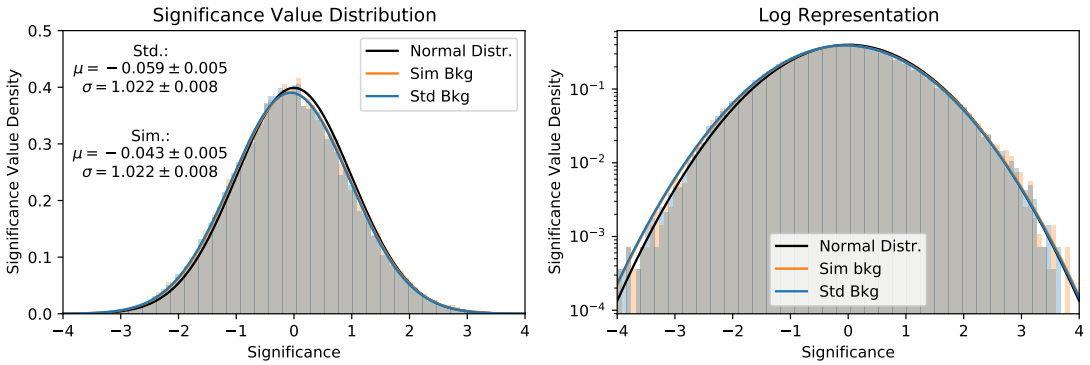

Figure 37: Significance value distribution of the spatial significance map for Cen A. The distribution is as expected. The small deviations from the normal distribution are similar to these of PKS 2155-304.

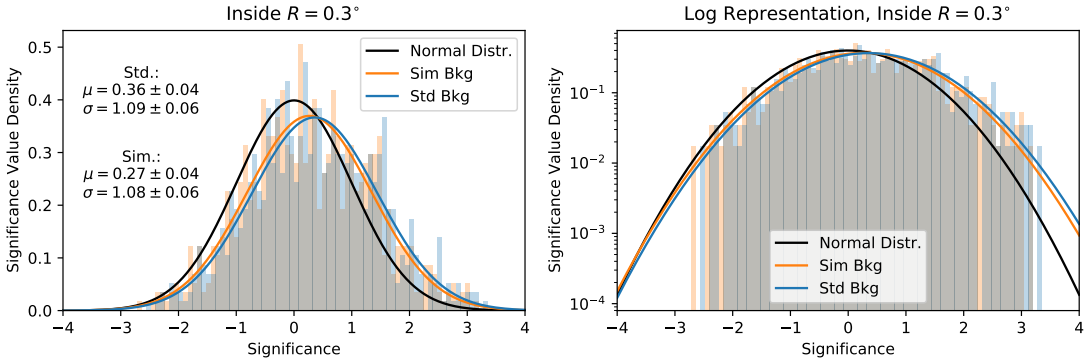

Figure 38: Significance value distribution for pixels with a FoV distance to the centre of less than 0.3°. The increased mean values are well visible.

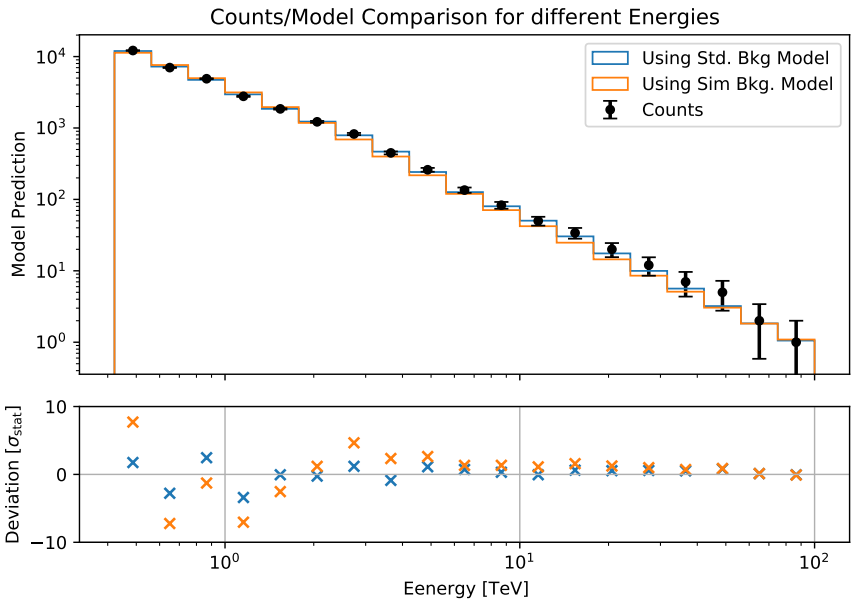

Figure 39: Energy dependent comparison between the predicted and measured number of counts. The error bars represent the Poisson uncertainty of the measurement. This uncertainty is for larger count rates proportionally lower, leading to higher deviations in units of significances for lower energies. The prediction of the model using the standard background is superior.

4.2 Energy Dependent Comparison between Model and Data

One other important point is the agreement of the model with the data for different energies. As before, this can be compared by summing the predicted and the measured counts over the spatial axes. The resulting values can be seen in Figure 39. The standard background model reaches here a good agreement with the data, the simulated one shows more deviations. For Cen A, the agreement between the model predictions and the data is better than for PKS2155-304. This can also be seen by looking at the distribution of the observed deviations, as shown in Figure 40. The model using the standard background shows a more compact significance distribution, the simulated one has more outliers. This can also be seen by the estimated systematical error δ_{bg}: For the model using the standard background this value is with $\delta_{\mathrm{bg}} = 1.5\,\%$ almost zero. The value of δ_{bg} using the simulated background is higher, here the systematical error is $9.7\,\%$. Both errors are lower than for PKS 2155-304. However, it is unclear if this is caused by the weaker gamma source.

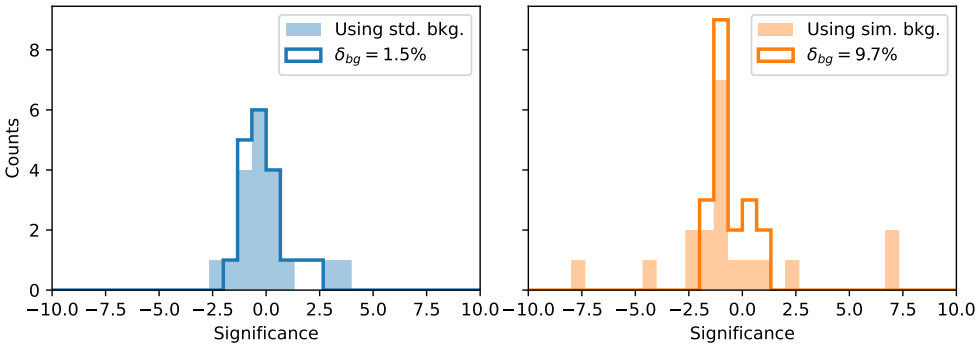

Figure 40: Histogram of the observed deviations. The model using the standard background shows less deviations, the one using the simulated background has more outliers. For the standard background, the systematical error is with 1.5 % very low, for the simulated one it is 9.7 %. Both errors are smaller than for PKS 2155-304.

4.3 Source Model and Flux Points

In this section, the two source models should be tested and compared. This can be done by using flux points. For PKS 2155-304, upper limits were used instead of flux points if the significance of the source model is for this energy bin lower than 2σ. As Cen A is with a source significance of 3.61/3.33 (std. / sim.) considerably weaker than PKS 2155-304, it was decided to only plot upper limits if the significance in this energy bin is below 1σ. This is shown in Figure 41. In general, both models are describing the respective flux points well. The simulated background analysis contains one upper limit, located at an energy of approximately 1 TeV. The significance values for the energy bins (E_{low} to E_{high}) are the following:

	Significance of source model in energy bin								
E_{ref} [TeV]	0.56	1.00	1.78	3.16	5.62	10.0	17.8	31.6	56.2
Using std. bkg.	2.04	1.18	2.21	1.01	2.12	-8.58	-5.11	-7.02	-4.44
Using sim. bkg.	1.98	0.57	2.01	1.23	2.23	-6.83	-14.3	-7.03	-4.43

In this table, E_{ref} is the logarithmic centre between E_{low} and E_{high}. For higher energies, the significance values get negative for both models. This happens when the fitted amplitude of the source model is negative for this energy bin, showing that the predicted background for the source region is too high in these energies. Because of the logarithmic scale, these flux points cannot be seen in Figure 41. The two largest deviations between the models using the standard and simulated background are in the energy bins 1.00 TeV and 17.8 TeV, showing that the simulated and standard background model are deviating in this energy bins. The low significances and the resulting large uncertainty of the models and flux points is caused by the weak gamma source and are therefore expected.

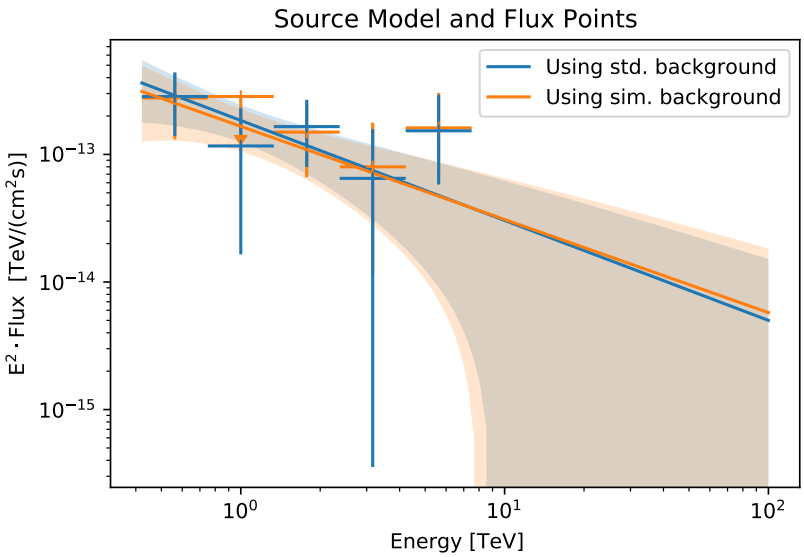

Figure 41: Flux points in combination with the two source models for Cen A. The flux points are in good agreement with one another. However, the model significances for the energy bins around 1.00 TeV and 17.8 TeV are deviating, indicating also deviating background models for this energy ranges.

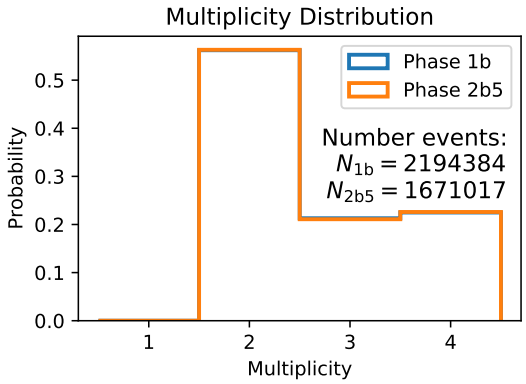

Figure 42: Multiplicity distribution of events from the optical phases 1b and 2b5. The two distributions are almost identical. The stated number of events can only be interpreted as an indication, because the computation power used for the two simulations was not necessarily identical. The lower number of counts of phase 2b5 is, because of the lower mean optical efficiency, expected.

5 Beyond the Scope of this Work

In the preparation for this thesis, also a diffuse γ-ray simulation for the optical phase 2b5 of H.E.S.S was made. The phase 2b5 depicts H.E.S.S in the time area 2015/2016, containing also the fifth telescope located at the centre of H.E.S.S. However, in this work, only the four small telescopes were considered. The optical efficiencies of the phases 1b and 2b5 can be found in the following table [33]:

	CT1	CT2	CT3	CT4
Phase 1b:	70 %	70 %	70 %	70 %
Phase 2b5:	63.3 %	62.9 %	58.6 %	73.8 %

This simulation did not find a place in the actual thesis, as the corresponding real observations of this phase does contain less suitable runs of the analysed point sources.

One main difference between the two optical phases is, that the optical efficiencies of the four telescopes are no longer uniform. This could influence the multiplicity distributions. These distributions are shown in Figure 42. The probability of a multiplicity of 3 is for phase 1b slightly higher, but overall are the two probability distributions of the two phases almost identical. The plot does also state the number of simulated events. However, this cannot be used to compare the count rates of the tow simulations, as it cannot be guaranteed that the used computation power for the two simulation was identical. Nevertheless, the observed trend, that phase 2b5 has less counts, is expected, as the mean optical efficiency of this phase is lower than that of phase 1b.

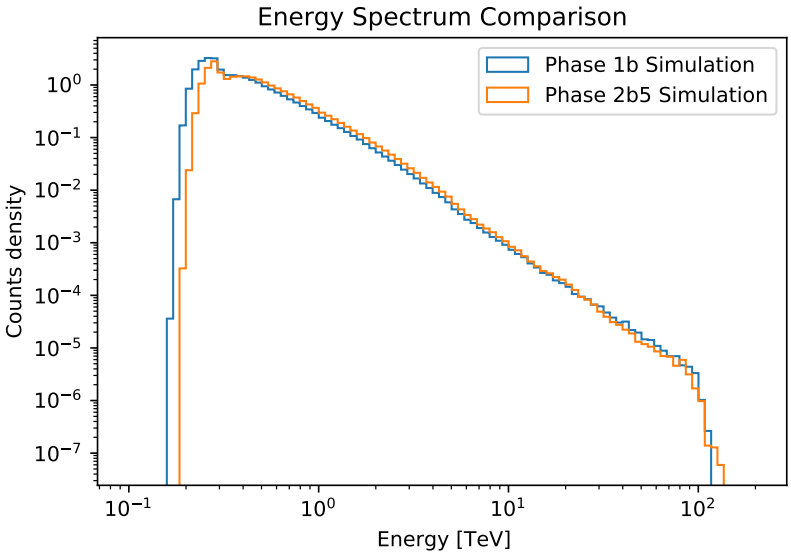

Figure 43: Energy spectrum comparison between phase 1b and 2b5 simulations. The distribution of the phase 2b5 simulation starts at a higher energy. It starts to decrease a bit later than 1b, but then it decreases slightly faster. However, phase 2b5 reaches higher energies than 1b.

Comparison of the Energy Spectrum

The energy spectra of the two simulations can be seen in Figure 43. The energy spectrum of phase 2b5 starts at a larger energy. This is expected, as the mean optical efficiency of this phase is lower. Therefore, more Cherenkov photons and thus a larger energy is needed to trigger a telescope. After the common peak energy, the begins to decrease later than phase 1b's spectrum. However, the spectrum of phase 2b5 is slightly decreasing faster than this of phase 1b. Finally, the spectrum of phase 1b is cut off at earlier energies. The reason for this is not apparent. However, for larger energies, the reconstruction of the primary energy gets more inaccurate. As most analyses stop at the latest at 100 TeV, this effect is not problematic.

Comparison of the FoV Distribution

In Figure 44 and Figure 45 the FoV distribution of the simulations of the two phases are compared. The shapes of the contour lines are very similar, both are of a circular shape. A more detailed comparison can be conducted by using the following comparison function:

$$\text{comparisonvalue} = 2 \cdot \frac{s - s'}{s + s'} \tag{18}$$

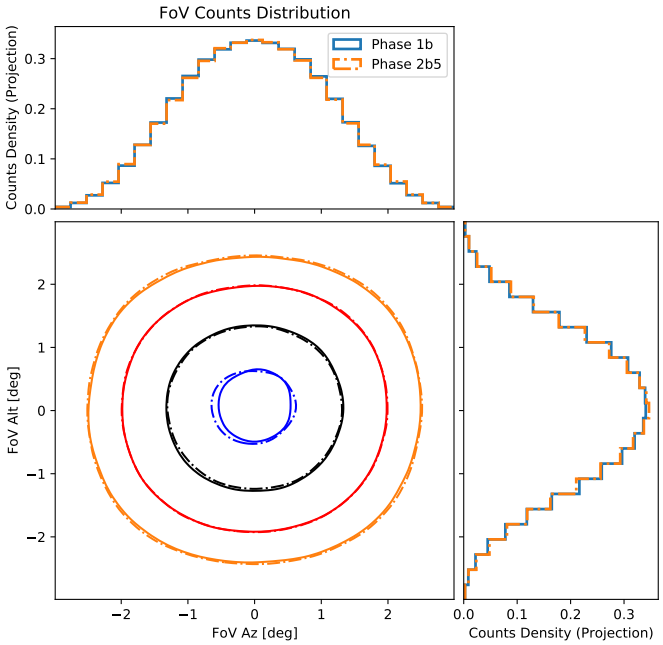

Figure 44: Contours of the FoV event distributions of the phases 1b and 2b5. Both distributions are very similar.

In this equation, s is the counts density of the phase 1b simulation, s' is the counterpart of phase 2b5. For two consistent distributions, this value should be zero. It can be seen that the distribution of phase 1b is higher at a distance to the FoV centre of 1°. At the FoV edge regions, it is lower. Furthermore, a gradient of the comparison function in the altitude direction can be observed. One explanation for this could be the decreasing number of detectable Cherenkov photons at lower altitudes. This effect is influencing the optical phase 2b5 stronger, as its optical efficiency is lower. As no rate information from these simulations is available, the number of detected events cannot be compared.

A comparison using four energy bins is shown in Figure 46. Besides small deviations between the first (0.10 TeV to 0.68 TeV) and the second energy bin (0.68 TeV to 4.65 TeV), the results are as expected.

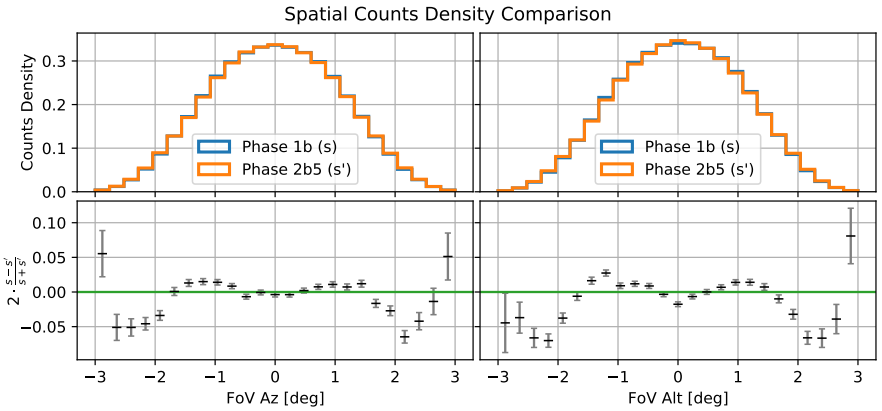

Figure 45: Deviations between the FoV distribution, depicted by using a comparison function. At a FoV distance of 1° to the centre, the counts density of phase 1b is higher. Towards the FoV edges, it is lower than this of phase 2b5. As no information about the rate is available, the overall number of detected events cannot be compared.

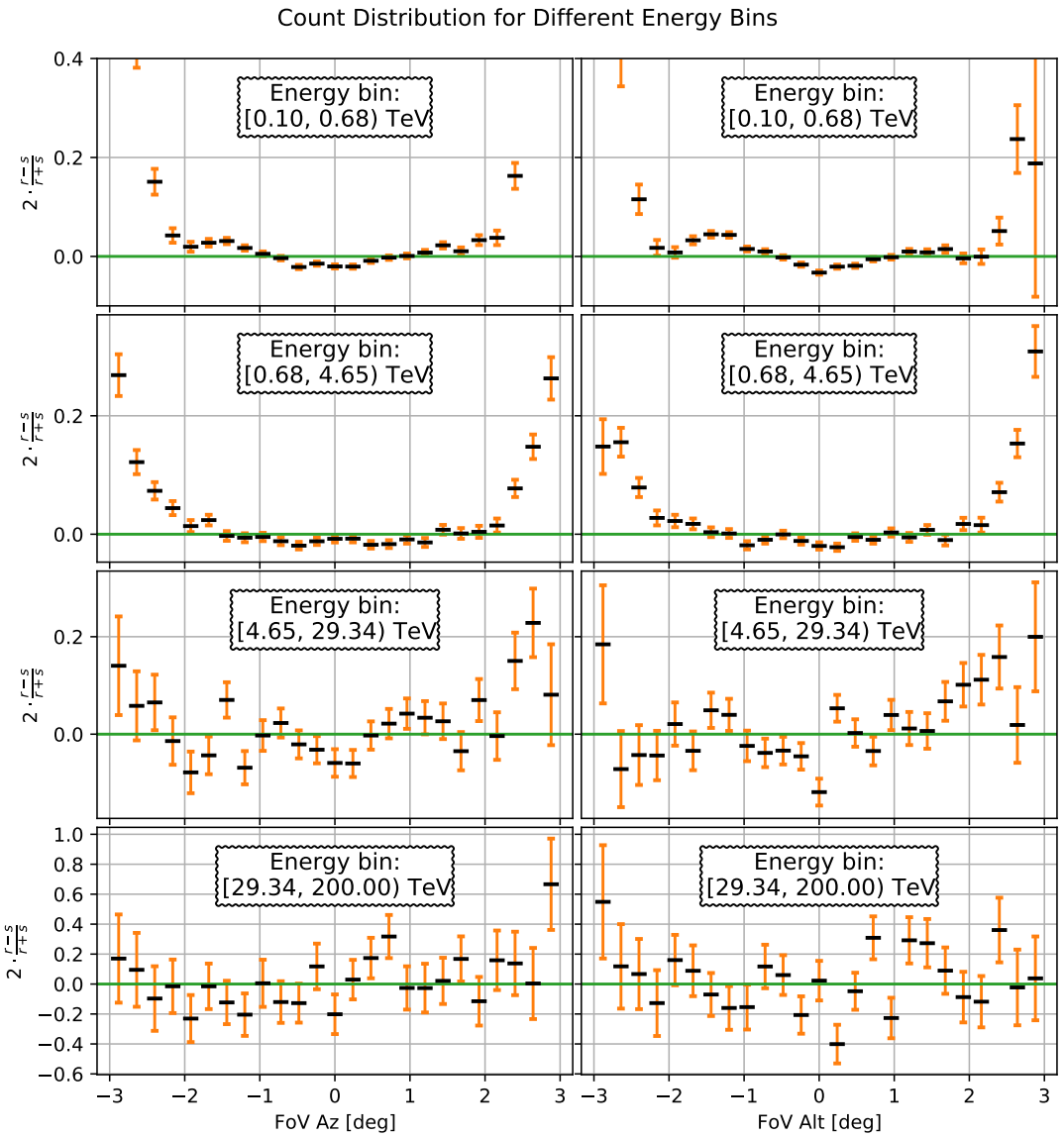

Figure 46: Comparison between the FoV distribution of the phase 1b and 2b5 simulation. There are small deviations between the first and second energy bin.

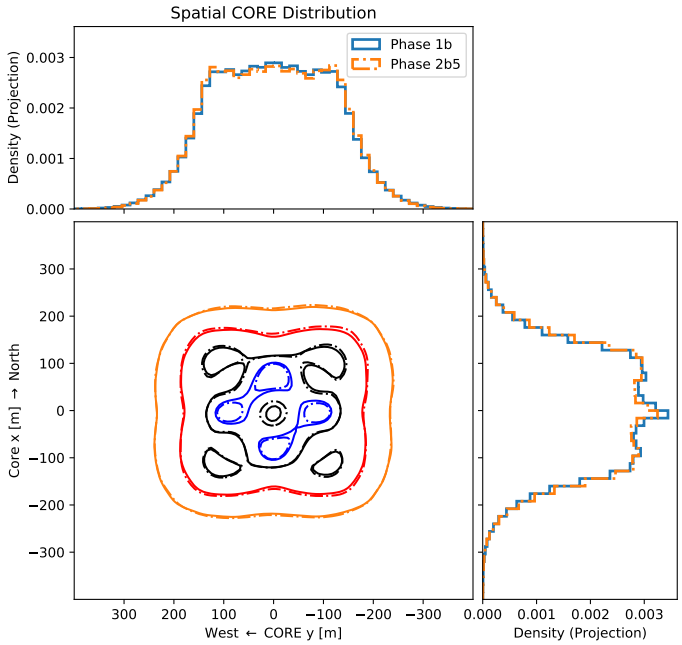

Figure 47: CORE distribution comparison between phase 1b and 2b5 events. The shapes of the two distributions are very similar.

Comparison of the CORE Distribution

The two CORE distributions are shown in Figure 47. Both shapes are very similar. The four peaks depicted by the blue contour lines coincide with the simulated telescope positions. A quantified comparison using the comparison function $d = 2 \cdot \frac{s-s'}{s+s'}$ is shown in Figure 48. This function compares the distribution of the phase 1b simulation s with its phase 2b5 counterpart s'. The distribution of the phase 2b5 simulation is in the centre region lower, and in a distance of 150 m to §150m higher than that of the phase 1b simulation.

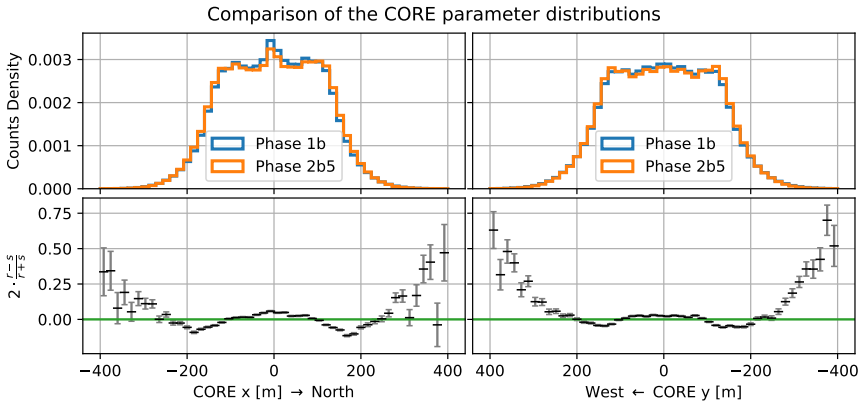

Figure 48: Deviations between the two CORE distributions, depicted by using a comparison function. The counts density of phase 1b is higher at the centre and the FoV edge regions. The difference between the CORE x and y distribution can be explained by the simulation pointing of az = 180°.

6 Summary and Outlook

This work aimed to construct a background model using simulated diffuse γ rays and assess its performance. It was shown that in general, these simulations are indeed able to model the background of the H.E.S.S telescope. However, there are some deviations. On the one hand, there is the unequal behaviour of the simulated and real energy spectrum at the BDT training bin edges. This is caused by the concept of using diffuse γ-rays. Therefore, it can only be attempted to correct this when the background model is constructed. The main problem is here the bin edge at 5 TeV. On the other hand, there are differences in the multiplicity distributions and a deviating minimum energy detection threshold. These deviations could possibly be decreased by adapting the H.E.S.S model used by the simulation. The relevant parameters are here the optical efficiencies and the dead-times of the cameras. Additionally, deviations of the CORE and FoV distributions were observed. It was shown that manually correcting the multiplicity could reduce the FoV deviations for all but the lowest energies. If an adaption of the simulation is not possible or successful, a manual energy dependent correction of the multiplicity could help to improve the resulting background model.

The second part of this thesis was to test the performance of the simulated background model in Gammapy point-source analyses. At first, this was done for PKS2155-304. This strong γ source was used to test the general ability of the simulated background to be used in a practical application. The simulated background could not reach the accuracy of the standard one. This was especially the case, if the energy dependent predictions of the model were compared with the data. These deviations were used to estimate a statistical error of the combined source and background model. A value of 11.7 % was obtained for the standard model, 26.7 % for the simulated one. A comparison of the spatial predictions was also carried out. There, a FoV centre to edge gradient was found for both background models. However, the obtained analysis parameters were in agreement with the standard analysis. Also, the confidence contours of the amplitude and spectral index of the source were matching.

Subsequently, an analysis of Centaurus A was conducted. This source is more difficult to analyse, as it is around 15 times weaker than PKS 2155-304. The standard background model was also here superior. The found problems were similar to that of the first analysis. One problem is the FoV edge to centre gradient which was observed for both the standard as well as the simulated background analysis. As the characteristic of this effect is like before, a problematic source model as cause seems to be unlikely. The energy dependent deviations were here lower than for PKS 2155-304. The statistical error of the combined source and background model was 1.5 % for the standard and 9.7 % for the simulated one. As this source is weaker, the calculated statistical should be less influenced by possible source model errors. Consequently, this value should depict the statistical error of the background model better. As before, the found parameters of the source model and their confidence contours are similar.

Beyond the scope of this work, diffuse γ simulations of the optical phases 1b and 2b5 were compared. It is shown that changing the optical phase is not limited to a changed normalisation but has various effects. Consequently, it could be considered to construct background models for individual optical phases.

In conclusion it can be said that this thesis proves the general ability of the simulated background model to depict the observed background and shows that they can be used for Gammapy analyses of point-like γ sources. However, the constructed background model has still weaknesses which need to be further addressed. This includes a more elaborate estimation of the existing statistical uncertainties. Furthermore, it has to be investigated if simulated background models can also be used for expanded sources.

7 Index of Abbreviations

BDT	Boosted Decision Trees
Cen A	Centaurus A
CTA	Cherenkov Telescope Array
Fermi	Fermi Gamma-ray Space Telescope
FoV	Field of View
H.E.S.S	High Energy Stereoscopic System
IACT	Imaging Atmospheric Cherenkov Technique
IRF	Instrument Response Function
KDE	Kernel Density Estimation
LIGO	Laser Interferometer Gravitational-Wave Observatory
MRSL	Mean Reduces Scaled Length
MRSLO	Mean Reduces Scaled Length Off
MRSW	Mean Reduced Scaled Width
MRSWO	Mean Reduced Scaled Width Off
PDF	Probability Density Function
PSD	Point Spread Function
VHE	Very High Energy

References

[1] Mohrmann, L. et al. "Validation of open-source science tools and background model construction in astronomy". In: *A&A* 632 (2019), A72. DOI: 10.1051/0004-6361/201936452.

[2] W. Heitler. *The Quantum Theory of Radiation*. Dover Books on Physics. Dover Publications, 1984. ISBN: 9780486645582.

[3] Thomas K. Gaisser, Ralph Engel, and Elisa Resconi. *Cosmic Rays and Particle Physics*. 2nd ed. Cambridge University Press, 2016. DOI: 10.1017/CBO9781139192194.

[4] Stefan Funk. "Ground- and Space-Based Gamma-Ray Astronomy". In: *Annual Review of Nuclear and Particle Science* 65.1 (Oct. 2015), pp. 245–277. ISSN: 1545-4134. DOI: 10.1146/annurev-nucl-102014-022036.

[5] S. Ohm, C. van Eldik, and K. Egberts. "γ/hadron separation in very-high-energy γ-ray astronomy using a multivariate analysis method". In: *Astroparticle Physics* 31.5 (2009), pp. 383–391. ISSN: 0927-6505. DOI: 10.1016/j.astropartphys.2009.04.001.

[6] Christian99. *H.E.S.S. II Telescope Array*. CC BY-SA 3.0.

[7] F. Aharonian et al. "Observations of the Crab nebula with HESS". In: *Astronomy & Astrophysics* 457.3 (Sept. 2006), pp. 899–915. ISSN: 1432-0746. DOI: 10.1051/0004-6361:20065351.

[8] M. Barrantes et al. "Atmospheric corrections of the cosmic ray fluxes detected by the Solar Neutron Telescope at the Summit of the Sierra Negra Volcano in Mexico". en. In: *Geofisica internacional* 57 (Dec. 2018). CC BY-NC-ND 3.0, pp. 253–275. ISSN: 0016-7169. URL: http://ref.scielo.org/8dqy78.

[9] Mathieu De Naurois. "Very High Energy astronomy from H.E.S.S. to CTA. Opening of a new astronomical window on the non-thermal Universe". Habilitation à diriger des recherches. Université Pierre et Marie Curie - Paris VI, Mar. 2012. URL: https://tel.archives-ouvertes.fr/tel-00687872.

[10] P.A. Zyla et al. (Particle Data Group). *Review of Particle Physics*. 2020. DOI: 10.1093/ptep/ptaa104.

[11] Heinrich J. Völk and Konrad Bernlöhr. "Imaging very high energy gamma-ray telescopes". In: *Experimental Astronomy* 25.1-3 (Mar. 2009). CC BY-NC 2.0, pp. 173–191. ISSN: 1572-9508. DOI: 10.1007/s10686-009-9151-z.

[12] A. M. Hillas. "Cerenkov Light Images of EAS Produced by Primary Gamma Rays and by Nuclei". In: *19th International Cosmic Ray Conference (ICRC19), Volume 3*. Vol. 3. International Cosmic Ray Conference. Aug. 1985, p. 445.

[13] Johannes Veh. "Dark Matter γ-line search in the Galactic Centre with H.E.S.S. using an On-Off technique". PhD thesis. Friedrich-Alexander University Erlangen-Nuremberg, July 2018.

[14] S. Ohm, C. van Eldik, and K. Egberts. "γ/hadron separation in very-high-energy γ-ray astronomy using a multivariate analysis method". In: *Astroparticle Physics* 31.5 (2009). With permission of Elsevier, pp. 383–391. ISSN: 0927-6505. DOI: 10.1016/j.astropartphys.2009.04.001.

[15] D. Berge, S. Funk, and J. Hinton. "Background modelling in very-high-energy ronomy". In: *Astronomy & Astrophysics* 466.3 (May 2007), pp. 1219–1229. DOI: 10.1051/0004-6361:20066674.

[16] D. Heck et al. *CORSIKA: A Monte Carlo Code to Simulate Extensive Air Showers.* Forschungszentrum Karlsruhe. 1998.

[17] Konrad Bernlöhr. "Simulation of imaging atmospheric Cherenkov telescopes with CORSIKA and sim_telarray". In: *Astroparticle Physics* 30.3 (2008), pp. 149–158. ISSN: 0927-6505. DOI: 10.1016/j.astropartphys.2008.07.009.

[18] H.E.S.S. Collaboration et al. "The H.E.S.S. Galactic plane survey". In: *A&A* 612 (2018), A1. DOI: 10.1051/0004-6361/201732098.

[19] Johannes Veh. "Stude der Pointing-Korrekturen von H.E.S.S. I". MA thesis. Friedrich-Alexander-Universität Erlangen-Nürnberg, 2013.

[20] Aharonian, F. et al. "H.E.S.S. observations of PKS 2155-304". In: *A&A* 430.3 (2005), pp. 865–875. DOI: 10.1051/0004-6361:20041853.

[21] C. Deil et al. "Gammapy - A prototype for the CTA science tools". In: *35th International Cosmic Ray Conference (ICRC2017)*. Vol. 301. Jan. 2017, p. 766. arXiv: 1709.01751 [astro-ph.IM].

[22] C. Nigro et al. "Towards open and reproducible multi-instrument analysis in gamma-ray astronomy". In: *Astronomy & Astrophysics* 625 (Apr. 2019), A10. ISSN: 1432-0746. DOI: 10.1051/0004-6361/201834938.

[23] Charles R. Harris et al. "Array programming with NumPy". In: *Nature* 585.7825 (Sept. 2020), pp. 357–362. DOI: 10.1038/s41586-020-2649-2.

[24] Pauli Virtanen et al. "SciPy 1.0: Fundamental Algorithms for Scientific Computing in Python". In: *Nature Methods* 17 (2020), pp. 261–272. DOI: 10.1038/s41592-019-0686-2.

[25] Astropy Collaboration et al. "Astropy: A community Python package for astronomy". In: *A&A* 558, A33 (Oct. 2013), A33. DOI: 10.1051/0004-6361/201322068. eprint: 1307.6212.

[26] Astropy Collaboration et al. "The Astropy Project: Building an Open-science Project and Status of the v2.0 Core Package". In: *The Astronomical Journal,* 156.3 (Sept. 2018), p. 123. DOI: 10.3847/1538-3881/aabc4f.

[27] *Gammapy Documentation.* https://docs.gammapy.org/0.18.2/index.html. Online, accessed 28-June-2021.

[28] W. Cash. "Parameter estimation in astronomy through application of the likelihood ratio." In: *The Astrophysical Journal* 228 (Mar. 1979), pp. 939–947. DOI: 10.1086/156922.

[29] S. S. Wilks. “The Large-Sample Distribution of the Likelihood Ratio for Testing Composite Hypotheses”. In: *The Annals of Mathematical Statistics* 9.1 (1938), pp. 60–62. DOI: 10.1214/aoms/1177732360.

[30] Andreas Specovius. “A new analysis of the PeVatron candidate HESS J1646-458 using a novel analysis technique”. urn:nbn:de:bvb:29-opus4-164536. Dissertation. Friedrich-Alexander-Universität Erlangen-Nürnberg (FAU), 2021.

[31] H. Abdalla et al. “Gamma-ray blazar spectra with H.E.S.S. II mono analysis: The case of PKS 2155-304 and PG 1553+113”. In: *Astronomy & Astrophysics* 600 (Apr. 2017), A89. ISSN: 1432-0746. DOI: 10.1051/0004-6361/201629427.

[32] H. Abdalla et al. “The γ-ray spectrum of the core of Centaurus A as observed with H.E.S.S. and Fermi-LAT”. In: *Astronomy & Astrophysics* 619 (Nov. 2018), A71. DOI: 10.1051/0004-6361/201832640.

[33] *Internal H.E.S.S Confluence Page*. Online, accessed 09-July-2021.

[34] J. D. Hunter. “Matplotlib: A 2D graphics environment”. In: *Computing in Science & Engineering* 9.3 (2007), pp. 90–95. DOI: 10.1109/MCSE.2007.55.

[35] Eric O. Lebigot. *Uncertainties: a Python package for calculations with uncertainties*. URL: http://pythonhosted.org/uncertainties/.

8 Acknowledgement

The plots in this thesis were generated by using Matplotlib [34]. Also the python packages [23], astropy [25], [26] and the uncertainties package [35] were used.

Danksagung

An dieser Stelle möchte ich mich bei Allen bedanken, die mich bei dieser Masterarbeit unterstützt haben. Insbesondere sind zu nennen:

- Prof. Dr. Christopher van Eldik für die Vergabe des Themas und für die zahlreichen Diskussionen, unter anderem in den wöchentlichen Meetings
- Prof. Dr. Stefan Funk für die Übernahme des Zweitgutachtens für diese Bachelorarbeit
- Andreas Specovius und Katrin Streil für die Beantwortung meiner Fragen
- Die Teilnehmenden der 3D-Analysis Meetings für die vielen Ideen
- Die gesamte Arbeitsgruppe für die allgemeine Hilfsbereitschaft

Vielen Dank an Ronja, dafür dass du mir immer zur Seite stehst.

Der größte Dank gilt meinen Eltern.

Erklärung

Hiermit bestätige ich, dass ich diese Arbeit selbstständig und nur unter Verwendung der angegebenen Hilfsmittel angefertigt habe.

Erlangen, den 11. Juli 2021

Marco Egelkraut